Journal of Non-Crystalline Solids 683 (2026) 124105

Contents lists available at ScienceDirect

Journal of Non-Crystalline Solids

journal homepage: www.elsevier.com/locate/jnoncrysol

Mechanisms of plastic deformation in pristine and pressure-densified sodium silicate and aluminosilicate glasses: A molecular dynamics investigation

Alfonso Pedone [a,*], Annalisa Pallini [a], Leopold Talirz [b], Wolfgang Mannstadt [b]

[a] Department of Chemical and Geological Sciences, University of Modena and Reggio Emilia, Modena, Italy
[b] SCHOTT AG, Mainz, Germany

ARTICLE INFO

Keywords:
Molecular dynamics simulations
Silicate glasses
Nanoindentation
Pressure effects

ABSTRACT

Understanding how glasses deform under sharp contact is essential for predicting and improving their resistance to surface damage and crack initiation. Here we use molecular dynamics simulations to examine nanoindentation in sodium silicate (NS) and sodium aluminosilicate (AL) glasses, both in pristine and pressure-densified states, with the aim of disentangling the relative contributions of densification and shear flow to plastic deformation. By resolving density and atomic free volume changes, stress and strain fields, atomic rearrangements and coordination defects around the indenter, we show that plasticity is strongly composition-dependent. In pristine NS, deformation is dominated by irreversible densification and persistent Si over-coordination localized beneath the indent. In contrast, AL glasses accommodate loading primarily through shear-mediated rearrangements of Al and Na, with $Al^{[5]}$, TBOs and Na coordination increasing during loading but largely recovering upon unloading. Pre-densification suppresses further volumetric compaction in both compositions and shifts the dominant mechanism toward shear flow, yielding broader non-affine displacement zones and a characteristic pile-up at the indent boundary. These results demonstrate that the balance between densification and shear is governed by the structural roles of Na and Al and can be tuned by pressure history. The mechanistic insights obtained here provide guidelines for designing silicate glasses with tailored resistance to surface damage and improved indentation response.

1. Introduction

Silicate glasses are widely used in applications where they are routinely exposed to concentrated mechanical contact, including scratch events, particle impacts, and indentation from sharp objects. Under such conditions, their response is governed by how the amorphous network accommodates plastic deformation at nanometric scales. Unlike crystalline materials, which deform via dislocation activity, amorphous oxide glasses lack long-range order and instead deform through a competition between two fundamental mechanisms: irreversible volumetric densification and non-affine shear flow. The balance between these pathways controls the size of residual imprints, the onset of surface flaws, and ultimately the resistance of glass to contact-induced damage [1–4].

The relative contributions of densification and shear flow vary significantly across glass families and depend sensitively on network topology, modifier content, and the availability of high-coordination structural states [5–12]. In silica-rich glasses, deformation under indentation or high pressure is known to proceed largely through densification, with persistent changes in density and network packing beneath the indenter [7,13–15]. Aluminosilicate glasses, by contrast, often undergo less permanent compaction and instead accommodate deformation through shear-assisted rearrangements, including reversible changes in aluminum coordination (e.g., formation of Al^5/Al^6 species) and local bond-switching events [6,12,16–20]. These differences arise from the distinct structural roles of Si, Al, and Na: Si^{4+} forms highly rigid tetrahedral networks that densify under pressure; Al can adopt multiple coordination states that promote angular flexibility; and Na^+ is a highly mobile modifier that enhances non-affine relaxation processes [21–24].

A number of studies have shown that pressure pre-densification is an effective route for strengthening silicate glasses, leading to enhanced

* Corresponding author.
E-mail address: alfonso.pedone@unimore.it (A. Pedone).

https://doi.org/10.1016/j.jnoncrysol.2026.124105
Received 18 September 2025; Received in revised form 7 February 2026; Accepted 4 April 2026
Available online 10 April 2026

hardness, reduced indentation depth, and improved resistance to contact damage [5,9,10]. Pre-densification accomplishes this by collapsing free volume, increasing network connectivity, and suppressing the formation of low-density structural motifs that otherwise promote densification-dominated plasticity. As a result, pre-densified glasses tend to exhibit a more shear-mediated deformation behaviour during indentation and show reduced residual densification on unloading [6,9,18,25–27]. However, most existing work has focused either on single-component or industrial glasses, and a mechanistic, atomistic comparison of how pre-densification modifies the plastic response of different compositions is still missing.

Thus, although indentation studies and high-pressure experiments have established that both composition and pressure history critically influence contact-induced deformation, the atomic-scale mechanisms through which pristine and pre-densified multi-component silicate glasses accommodate load—via densification, shear flow, or mixed modes—remain insufficiently understood. In particular, no unified framework has yet resolved how sodium silicate (NS) and sodium aluminosilicate (AL) glasses differ in their structural response to indentation, and how pre-densification tunes the availability of structural defects and deformation pathways during loading and unloading.

Atomistic simulation techniques—and molecular dynamics (MD) in particular—have become an essential tool for investigating deformation and structural modification in hard and brittle materials [11,12,28–37]. MD has been widely and successfully applied to diamond, silicon, and glass-ceramics to reveal nanoscale densification, shear flow, bond rearrangement, and the formation of modified layers under extreme mechanical or thermal loads. For example, Yuan et al. [38]. combined atomistic modelling with experimental analysis to elucidate the atomic-scale mechanism of modified-layer formation during laser–material interaction, demonstrating the ability of MD to capture the interplay between densification, local chemical effects, and shear-mediated rearrangements. These studies highlight the maturity and reliability of MD as a framework for resolving nanoscale deformation mechanisms in brittle solids, thereby providing a solid methodological basis for the present work.

In a previous work, we employed molecular dynamics (MD) simulations to study the bulk properties of sodium silicate with composition 12.5 %Na_2O·87.5 %SiO_2 (denoted NS hereafter) and aluminosilicate glass with composition 12.5 % Na_2O·12.5 % Al_2O_3·75 % SiO_2 (denoted AL hereafter) subjected to pressure-induced densification [39].

These compositions were chosen for their different responses to densification and their contrasting structural features: Na acts as a modifier in NS and as a compensating cation in AL. They provide a representative framework for understanding the effects of pressure treatment on bulk and surface behavior.

The results revealed that densification enhances stiffness and reduces the prevalence of non-bridging oxygens (NBOs) while promoting a more compact and interconnected network structure. These structural modifications were shown to improve the bulk mechanical performance of the glasses, as evidenced by increased elastic moduli and reduced residual densification during unloading. Building on these findings, the present study shifts focus to the structural variation occurring near the indenter during nanoindentation tests performed on pre-densified and pristine glasses, with an emphasis on the underlying mechanisms of densification and shear deformation.

In particular, key objectives of this study include:

1. Evaluating qualitatively and quantitatively the impact of pre-densification on surface hardness, plastic deformation mechanisms and elastic recovery.
2. Investigating the structural changes, such as atomic coordination and bond rearrangements, induced by nanoindentation and understanding the role played by Al when substituting Si in tetrahedral coordination and sodium when acting as compensator and modifying cation.
3. Analyzing the role of shear deformation in accommodating stress during indentation, with a focus on differences between pre-densified and pristine glasses.

Table 1
Glass compositions: percentage of oxides, number of atoms, density of final boxes.

	Na atoms	Al atoms	Si atoms	O atoms	Tot atoms	ρ (g^*cm^{-3})	L_{box} (Å)
AL	6152	6152	18,464	49,232	80,000	2.320	102.865
NS	5920	-	23,712	50,384	80,016	2.299	104.700

The remainder of this manuscript is organized as follows: In the next section we describe the computational methodology, including details of the MD simulations, glass preparation, surface characterization and nanoindentation protocol. Then we present the results, focusing on surface properties, structural differences between pre-densified and pristine glasses. Finally, we analyze and discuss the phenomena occurring around the indenter tip during indentation tests, highlighting the role of densification in modifying surface behavior and its relevance for practical applications.

2. Computational methods

The glass structures were generated using the traditional melt-quench approach via molecular dynamics simulations, using the LAMMPS code® [40]. We started by randomly placing the atoms in a cubic box whose side is related to the experimental density as reported in Table 1. The number of atoms contained in each box is 80,000 atoms for AL and 80,016 atoms for NS.

Then, the system is melted at 3000 K and kept at this temperature for 40 ps using the NVT ensemble and then rapidly cooled down at 300 K by applying a monotone cooling rate of 5 K/ps using the NPT ensemble (Nosé–Hoover) [41] with atmospheric pressure. Finally, the box is equilibrated at 300 K for 200 ps. The equation of motion was solved using the Verlet-Leapfrog algorithm with a time step of 0.002 ps. The BMP interatomic potential [42] has been used to describe atomic interactions because it reproduces well the structure and elastic properties of multicomponent oxide glasses [39,43].

It is based on the assumptions of rigid ion model and partial charges, and it describes the interactions between ions in a great number of multicomponent oxide-based systems [44–49]. BMP makes use of three different functional forms: a (Coulomb-)Morse potential (Eq. (1)), a Buckingham potential (Eq. (2)) and a three-bodies potential (Eq. (3)):

$$U^{C-M}(r_{ij}) = \frac{z_i z_j}{r_{ij}} e^2 + D_{ij}\left[\left(1 - e^{-a_{ij}\left(r_{ij}-r_{ij}^0\right)}\right)^2 - 1\right] + \frac{C_{ij}}{r_{ij}^{12}} \quad (1)$$

$$U^{B}(r_{ij}) = A_{ij}\cdot e^{\left(-\frac{r_{ij}}{\rho_{ij}}\right)} \quad (2)$$

$$U^{TBP-Screened}(\theta_{ijk}) = \frac{K_{ijk}}{2}\cdot\left(\theta_{ijk} - \theta_{ijk}^0\right)^2 \cdot e^{-\left(\frac{r_{ij}}{\rho}+\frac{r_{jk}}{\rho}\right)} \quad (3)$$

The (Coulomb-)Morse potential (Eq. (1)) describes the interactions between an oxide ion and cations and between two oxide ions and it is composed of three contributions. The first one accounts for long-range Coulombic interactions using partial and fixed charges (−1.2e for O, 2.4 for Si, 1.8 for Al and 0.6 for Na). The second one is a Morse potential describing short-range interactions via the parameters D_{ij} a_{ij} and r_{ij}^0 which regulates the depth of the potential well, curvature and the equilibrium distance. The third one is a repulsive term, which is useful to avoid atomic collapse at high-temperature and pressure. The Buckingham potential (Eq. (2)) is useful to describe repulsive interactions between former ions whereas the three-bodies potential (Eq. (3)) is a

screened harmonic function useful to describe Si-O-Si bond angle distributions. All the parameters are reported in Table S1 of the ESI.

The short-range interactions were evaluated using a cut-off of 7 Å whereas the long-range Coulombic interactions have been evaluated using the Ewald summation method with cut-off distances of 12 Å.

Densified glasses were created starting from structures generated at atmospheric pressure, subjecting them to high-pressures and high temperatures. The systems generated in the previous section are first relaxed for 20 ps at 50 K in the NVT ensemble and then heated to 1600 K in 100 ps using the NPT ensemble simultaneously increasing the pressure from 0 GPa to 1.5 GPa. The final temperature and pressure are maintained for 2 ns, after which the systems are cooled down from 1600 K to 50 K in 10 ns while maintaining the pressure at 1.5 GPa. In the next 4 ns, the pressure of the systems is reduced to its initial value (first 2 ns), and then the system is kept at these conditions for the remaining time.

From the bulk configurations, we generated two free surfaces by extending the simulation cell along the z-axis to introduce a vacuum region large enough to prevent interactions between periodic images. The resulting slab models were then replicated twice along both the *x* and *y* directions to obtain larger surfaces of approximately 200 Å lateral size, containing ~320,000 atoms. These extended slabs were subsequently relaxed and reconstructed through a heating–cooling equilibration cycle in the NVT ensemble to remove residual stresses and allow surface reconstruction. The system was first heated up from 300 K to 1600 K with a heating rate of 5K/ps and then cooled down from 1600 K to 300 K with the same rate, followed by equilibration at 300 K for 400 ps.

The surfaces were analysed by calculating the variation of the density, glass structure (atomic coordination numbers) and elemental composition along the z-direction. The atomic surface topography of the glass (roughness) was analysed using an areal approach derived from surface metrology standards. The outermost surface (20 Å) was discretized in the x-y plane into square bins of size of 2.0 Å x 2.0 Å because this is a minimum volumetric section that can contain at least one tetrahedral TO_4 unit (T = Si, Al). For each bin *(i,k)*, the maximum atomic height $h_{max}(i,k)$ was taken as the highest atomic z-coordinate within that region, generating an height map $h_{max}(x,y)$. A best-fit plane $h_{fit}(x,y) = ax + by + c$ was subtracted to remove global tilt, and the detrended height field $\bar{h}(x,y) = h_{max}(x,y) - h_{fit}(x,y)$ was used to compute roughness metrics. The arithmetic mean roughness $R_a = \langle|\bar{h} - \langle\bar{h}\rangle|\rangle$, the root-mean-square roughness $R_q = \sqrt{\left\langle(\bar{h} - \langle\bar{h}\rangle)^2\right\rangle}$ were evaluated. Additionally, we calculated the standard deviation of all h_{max} values $\sigma_{h_{max}} = \sqrt{\left\langle(h_{max} - \langle h_{max}\rangle)^2\right\rangle}$, representing the statistical dispersion of surface heights. These parameters correspond to the areal roughness descriptors defined in ISO 25,178–2 and their atomic scale analogues commonly used in AFM and atomistic modelling studies [50].

After a structural analysis of the pristine and pre-densified surfaces, we performed the indentation test and analysed the environment during the simulation path.

The nanoindenter tip was modelled as a conical body composed of carbon atoms arranged in a diamond lattice. The cone axis was oriented along the *z*-direction, with the apex positioned above the slab surface. The cone geometry was chosen to reproduce the equivalent contact area of a standard Berkovich pyramidal tip [51]. Following the classical conversion between the three-sided Berkovich geometry (65.3° face angle, 142.3° total included angle) and an axisymmetric cone providing the same projected contact area for a given penetration depth, the corresponding half-apex angle is 37.3°, equivalent to a total included angle of 74.6° For the selected base radius of 40 Å, this angle yields a cone height of approximately 52.5 Å. The final tip model contained 15,811 carbon atoms. The use of a conical model instead of the exact three-sided Berkovich pyramid allows one to preserve the correct contact area–depth relationship while ensuring axial symmetry, thus significantly reducing computational cost and facilitating the analysis of stress and strain fields beneath the indenter. A schematic representation of the nanoindentation setup is shown in Fig. 1.

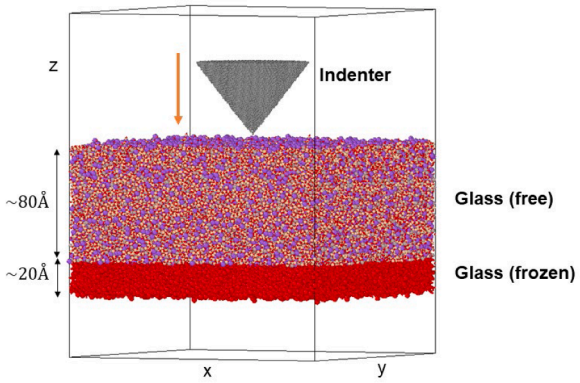

Fig. 1. Schematic representation of the nanoindentation set up.

The interactions between carbon atoms in the indenter were described using the Tersoff bond-order potential in the 1994 formulation of Tersoff, [52] as implemented in LAMMPS. The total energy is given by a sum over all atomic pairs: [53,54]

$$E = \sum_i \sum_{j>i} f_c(r_{ij}) \left[f_R(r_{ij}) - b_{ij} f_A(r_{ij}) \right] \tag{4}$$

Where the repulsive and attractive pair terms have exponential form:

$$f_R(r) = A exp(-\lambda_1 r), f_A(r) = B exp(-\lambda_2 r) \tag{5}$$

The cutoff function smoothly turn interactions off between radii R-D and R + D:

$$f_c(R) = \begin{cases} 1, & r < R - D \\ \frac{1}{2} + \frac{1}{2} cos\left[\frac{\pi(r - R + D)}{2D}\right] \\ 0, & r > R + D \end{cases} \tag{6}$$

The bond-order term introduces many-body and angular dependence:

$$b_{ij} = \left(1 + \beta^n \varsigma_{ij}^n\right)^{-1/2n} \tag{7}$$

With the angular environment function

$$\zeta_{ij} = \sum_{k \neq i,j} f_c(r_{ik}) g(\theta_{ijk}) \tag{8}$$

and

$$g(\theta) = \gamma \left(1 + \frac{c^2}{d^2} - \frac{c^2}{d^2 + (cos\theta - cos\theta_0)^2}\right) \tag{9}$$

This form enables the potential to capture the dependence of bond strength on local coordination and bond angles, reproducing the structural and mechanical behaviour of diamond and other carbon phases. The parameters are reported in Table S2 of the ESI. Finally, the tip-glass interactions have been modelled by using non-bonding Buckingham potential with A = 1000 eV, ρ=0.25 Å and C = 0 eV/Å^6.

This functional form was selected to prevent unphysical adhesion or charge transfer between the carbon tip and the glass surface, ensuring that the interaction is dominated by short-range Pauli repulsion upon contact. The chosen parameters produce a steep repulsive wall that effectively mimics the mechanical constraint of a hard, chemically inert diamond tip while avoiding unrealistic penetration or bonding to surface atoms. Similar purely repulsive potentials have been widely employed in nanoindentation simulations to approximate hard–soft material contacts where chemical interactions are negligible and the

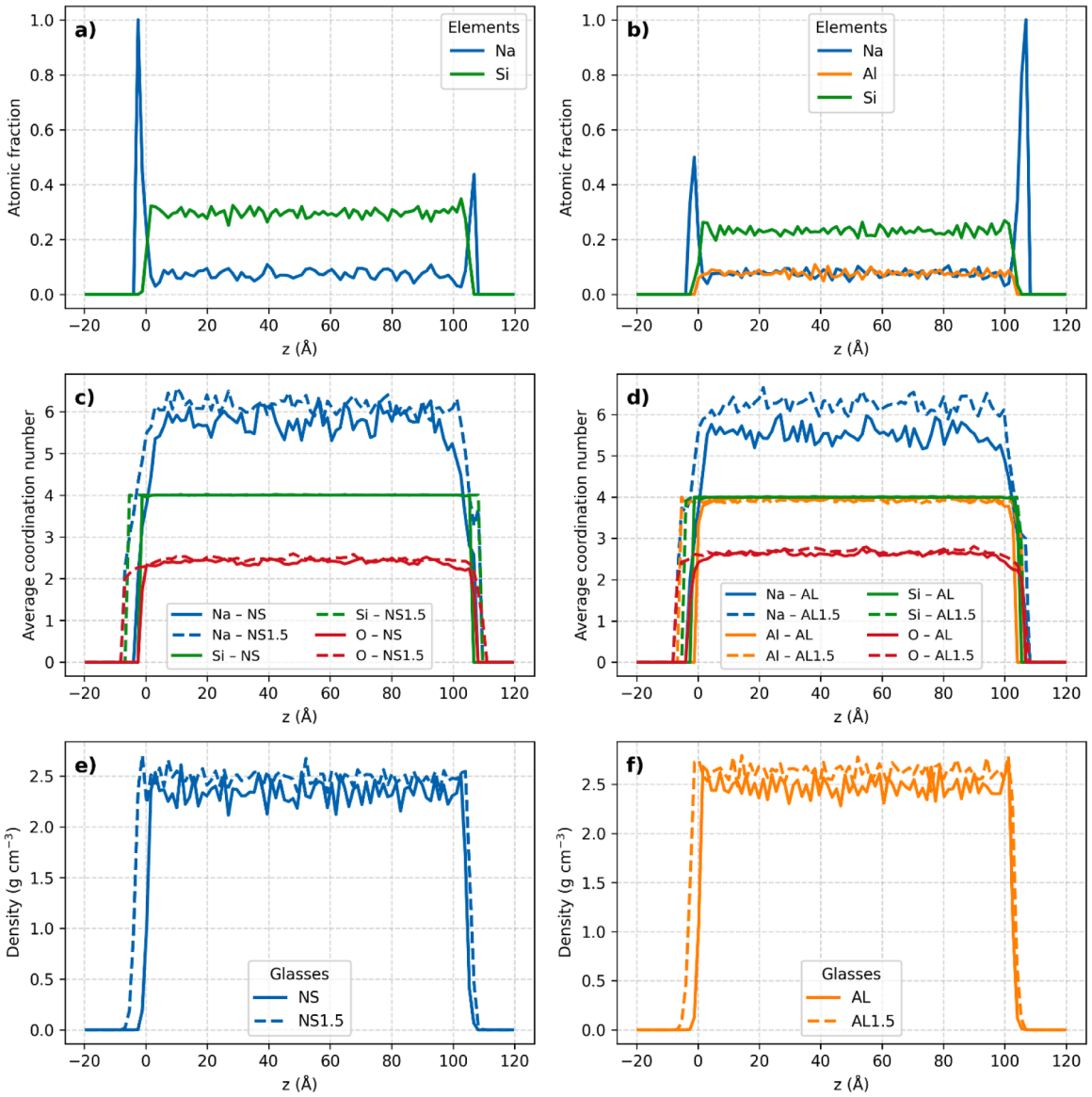

Fig. 2. Structural analysis along z axis for the four glass compositions investigated. (a) Atomic-fraction profiles of Na and Si across the NS slab; (b) Atomic-fraction profiles of Na, Al, and Si across the AL slab; (c) Coordination-number profiles of Na, Si, and O for NS (solid) and NS 1.5 (dashed) glasses; (d) Coordination-number profiles of Na, Al, Si, and O for AL (solid) and AL 1.5 (dashed) glasses; (e) Density profiles for NS and NS1.5 glasses. (f) Density profiles for AL and AL1.5 glasses. Solid and dashed lines distinguish the pristine and densified glasses, respectively; colours correspond to chemical elements in panels (a–d) and to glass labels in panels (e,f).

main effect of the indenter is to impose a local mechanical load [11,19].

The indentation was simulated in NVT ensemble at a constant temperature of 300 K lowering the tip along the *z*-axis with a rate of 0.5Å/ps until the entire 5 nm tip penetrated the glass surface. Before unloading the tip was held at the maximum penetration for 100 ps. Finally, the tip has been unloaded with the same velocity. During the simulations the atoms in the bottom layer (20 Å) of the glass have been fixed. Long-range electrostatic interactions were treated using the Damped Shifted Force (DSF) method, which provides a real-space description with continuous energy and forces without the need for Ewald summation [55]. For validation purposes, additional simulations were performed using the Wolf summation method, [56] yielding results indistinguishable within statistical uncertainty (see Figure S1 of the ESI).

To assess the influence of the penetration rate, additional nano-indentation tests were performed on the smaller albite slab model (≈ 80k atoms) using a conical tip of 25 Å height and 20 Å basal radius. Two loading velocities of 0.1 and 0.5 Å ps^{-1} where tested. The resulting loading and unloading force–displacement curves (reported in Figure S2 of the ESI) almost completely overlap and exhibit identical maximum loads at the same penetration depth. Moreover, the hardness values calculated using the Oliver and Pharr method (see below) are indistinguishable within numerical uncertainty. These results indicate that the indentation response is rate-independent within this range, allowing the use of the highest rate (0.5 Å ps^{-1}) for the larger production systems to reduce computational cost. Comparable loading rates (0.1–0.5 Å ps^{-1}) have been widely adopted in previous molecular-dynamics nano-indentation studies to balance physical realism and simulation efficiency [11,12,31,57].

Two methods have been used to estimate the Hardness. The Oliver and Pharr method [58] and the is used to determine the hardness since does not involve the area of the *indentation*, which is ill defined at the nanoscale.

Hardness is defined as the ratio between the maximum load (P_{max}) over the *contact* area (A_c) between indenter and the glass:

$$H = \frac{P_{max}}{A_c} \tag{10}$$

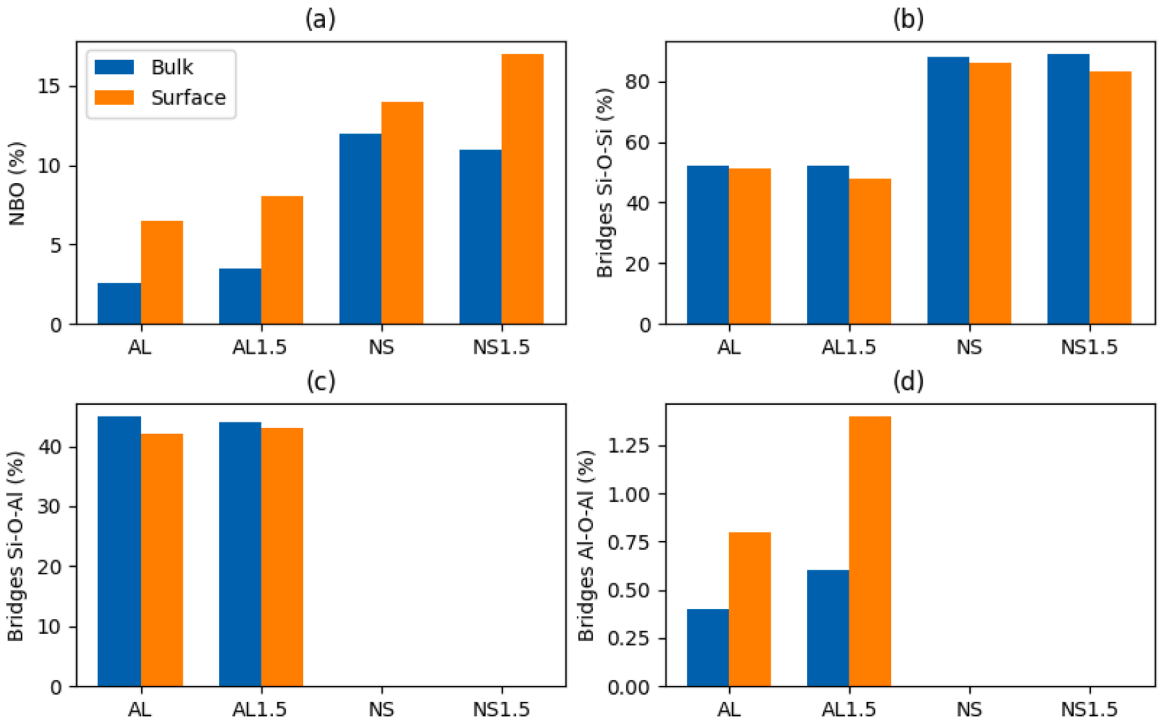

Fig. 3. Population of NBOs (a), Si-O-Si (b), Si-O-Al (c) and Al-O-Al (d) bonds in the bulk and at the surface of the investigated glasses.

In the present work, $A_c$was evaluated using two alternative approaches. The first approach is the Oliver and Pharr method [58] for which the projected contact area of a conical indenter with apex angle φ is given by:

$$A_c = 4h_c^2 tan^2(\varphi/2) \tag{11}$$

where h_c is the contact depth, computed as:

$$h_c = h_{max} - \varepsilon\frac{P_{max}}{S} \tag{12}$$

Here h_{max} is the maximum penetration depth, ε is a geometry-dependent constant (ε = 0.72 for a conical indenter), and S is the contact stiffness, defined as the slope of the unloading curve at maximum load, $S=(dP/dh)_{Pmax}$. The unloading branch was fitted using the functional form:

$$P = a(h - h_f)^m \tag{13}$$

Where h_f is the residual indentation after unloading, and *a* and *m* are the fitting parameters.

In addition to the Oliver–Pharr procedure, we also estimated the hardness using a complementary geometrical approach that does not rely on continuum contact mechanics assumptions. This alternative method is motivated by the atomistic nature of the simulations and by the fact that, after unloading, the indenter is no longer in contact with the glass surface. As a consequence, the contact area cannot be defined directly and must instead be inferred from the geometry of the residual indentation imprint.

In this second approach, the residual indentation cavity is approximated as a right circular cone whose geometry is defined by the shape of the indenter and by the residual indentation depth h_f. As stated above, the conical indenter used in the simulations has a total height $H_0 = 52.5$ Å and a basal radius R_0=40 Å. Assuming geometrical similarity between the indenter and the residual imprint, the effective base radius r_f of the residual cavity is obtained as $r_f=R_0h_f/H_0$. The characteristic area associated with the residual imprint is then approximated by the lateral surface of this cone, excluding the base, and is computed as:

$$A_c = \pi r_f\sqrt{r_f^2 + h_f^2} \tag{14}$$

This geometrical definition provides a conservative, atomistically grounded estimate of the characteristic area over which the maximum load is distributed. The corresponding hardness, is therefore not intended to replace the Oliver–Pharr value, but rather to provide an alternative estimate that is better suited to the angstrom-scale resolution of molecular-dynamics simulations and that enables a more direct comparison with experimental hardness values.

Local continuum fields (density, stress and strain maps) during indentation tests were computed by binning atomistic data with LAMMPS (chunk/atom + bin/3d command) and by extracting a mid-x yz-slice of fixed thickness (10 Å). For the production runs we adopted a bin size of 2 × 2 × 2 Å^3. This choice was motivated by two points: (i) it is comparable to the typical atomic length scale in silicate networks (the Si–O first-neighbour distance is ≈1.6 Å and the coordination cutoff commonly used for Si is 2.0 Å), therefore a 2 Å bin typically samples at least one SiO_4 tetrahedron on average; (ii) it provides a good compromise between spatial resolution and statistical averaging over a sufficient number of atoms per bin. We performed a convergence test by recomputing the post-unload densification maps for the AL composition with several dx = dy values (see Figure S3 of the ESI). The maps show that the spatial pattern, peak densification values and overall extent of the densified zone are stable for bin widths around 2 Å; reducing the bin width increases small-scale noise, while larger bins smooth fine features but do not change the main conclusions.

3. Results and discussions

3.1. Surface properties: composition, density and roughness analysis

In this section we describe the structural analysis of the glass surfaces before indentation experiments. The molar fraction of Na, Si and Al along the z-direction for the NS and AL glasses are shown in Fig. 2(a and b). The analogous data are not reported for the pre-densified NS1.5 and AL1.5 glasses because we did not observe appreciable differences.

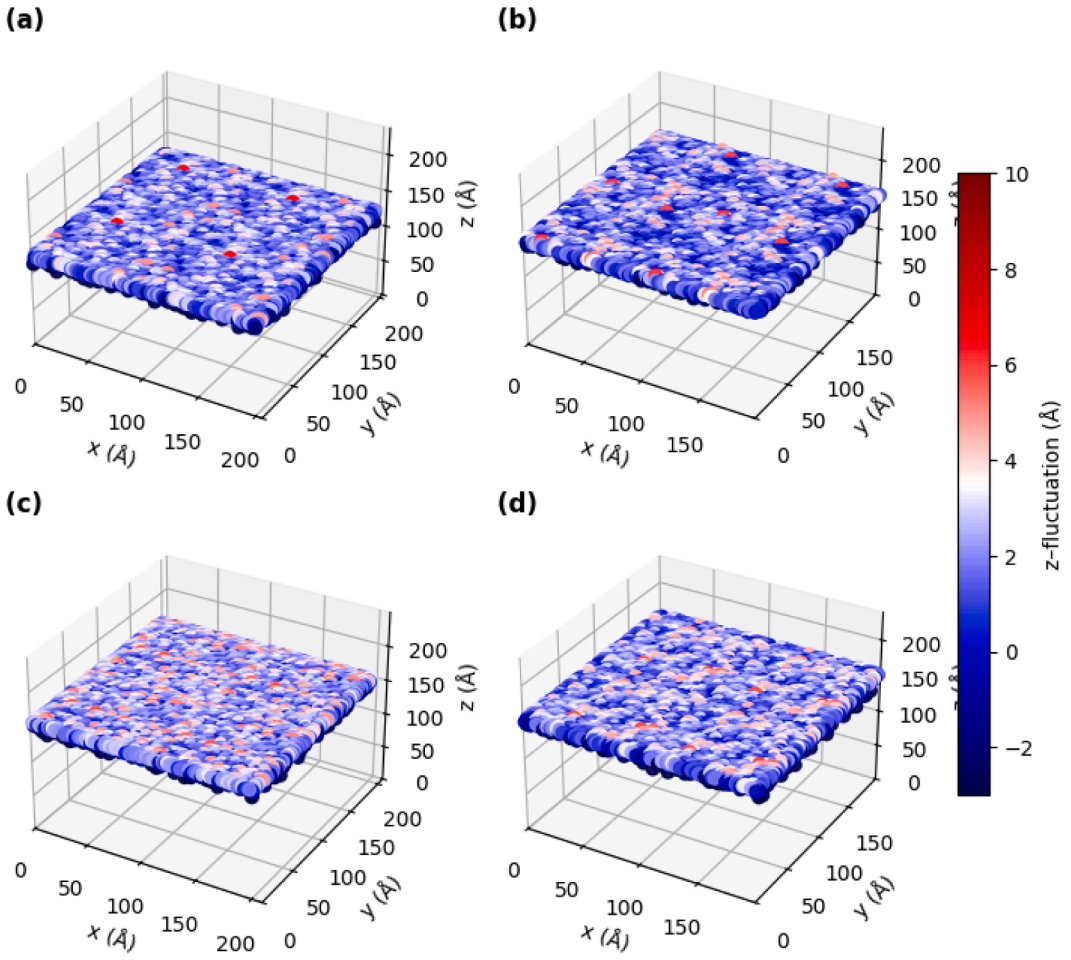

Fig. 4. Surface image analysis focused on both surfaces of each glass sample: a) AL glass, b) AL 1.5 glass, c) NS glass, d) NS 1.5 glass. The plots show the fluctuation of the z coordinate for each atom of the surfaces. Negative values refer to fluctuations towards the inside of the box, positive values to fluctuations towards the outside of the box.

Considering the region where the atomic fractions stabilize to the bulk one, we identify a surface thickness of about 10 Å. The analysis reveals that the surfaces of all the glasses are enriched in sodium ions. These results align with experimental studies using ion scattering spectroscopy, which also reported an increase in sodium concentration at glass surfaces [59,60].

The z-profiles for Si show that its molar fraction at the glass surface (just below the sodium layer) is slightly higher than in the bulk, forming small peaks at approximately 0 and 100 Å. In contrast, Al does not exhibit such peaks, indicating that its molar fraction at the glass surface closely matches that in the bulk.

These findings suggest that Al does not preferentially accumulate at the surface or subsurface layers but it is mixed with Si as in the bulk.

The coordination number profiles reported in panels c) and d) shows that Si and Al are 4-coordinated along the whole slab models both for pristine and pre-densified glasses. As for Na, the coordination number is lower at the surface for all glasses compared to the bulk. For the AL glass, the average coordination number of Na in the first 10 Å of the surface is approximately 5.5 and increases to about 5.8 after densification. A similar increment from 5.8 to 6.4 is observed in the bulk. Similarly, the average coordination number of Na of NS glass shows an increase from 4.6 to 5.2 upon densification at the surface and from 5.8 to 6.2 in the bulk. This increase in coordination number reflects the densification of the glass structure under pressure.

The density profiles reported in panels e) and f) of Fig. 2 shows that application of a pressure of 1.5 GPa induces densification of approximately 5 % for the NS glass and 6.6 % for AL glass. Specifically, the surface density of the AL glass increases from 2.382 g/cm^3 to 2.540 g/cm^3, while for the NS glass, it increases from 2.280 g/cm^3 to 2.403 g/cm^3.

Table 2
Surface roughness parameters of aluminosilicate (AL) and sodium-silicate (NS) glasses before and after densification under 1.5 GPa. R_a is the arithmetic mean roughness, R_q the root-mean-square roughness, and σ_{hmax} the standard deviation of the height map maxima, all expressed in nm.

	R_a (nm)	R_q (nm)	σ_{hmax} (nm)
AL	0.208	0.277	0.278
AL 1.5	0.194	0.261	0.262
NS	0.238	0.317	0.318
NS 1.5	0.217	0.289	0.289

The population of NBOs, Si-O-Si, Si-O-Al and Al-O-Al bonds at the surface and in the bulk of the glasses investigated are reported in Fig. 3.

In general, the population of NBOs is higher at the glass surface than in the bulk in agreement with the observation of sodium enrichment. As expected, the percentage of NBOs is higher in the NS glass than the AL one, the latter having a tectosilicate composition. The amount of NBOs at the glass surface slightly increases with pre-densification.

For the AL glass we observe a slight reduction of the amount of the Si-O-Si and Si-O-Al bonds at the glass surface with respect to the bulk which is compensated by the formation of more Al-O-Al bonds denoting a more pronounced tendency of aluminum to aggregate at the surface. This aggregation is enhanced by pre-densification.

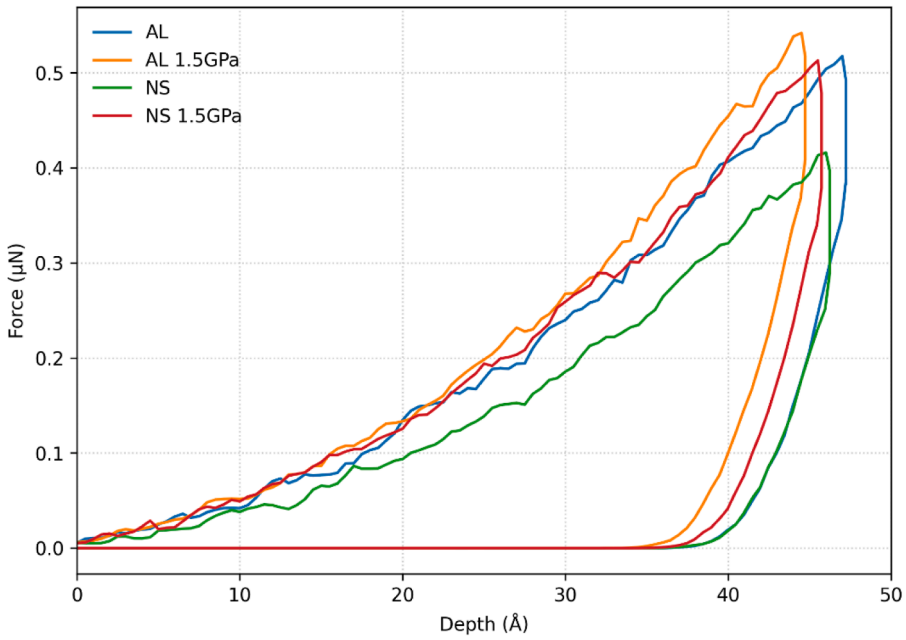

Fig. 5. Load vs Displacement curves for all investigated glasses during loading and unloading.

Fig. 4 shows the atoms on the glass surface with the maximum z-coordinate, mapped using a grid in the *xy* plane with a resolution of about 2.0 Å x 2.0 Å.

Table 2 reports the arithmetic (R_a), root-mean-square (R_q), and standard-deviation (σ_{hmax}) roughness values for the pristine and pre-densified glass surfaces as defined in the section of the computational methods. All values are below 0.3 nm (< 3 Å), which is consistent with atomically smooth, relaxed surfaces generated in Molecular Dynamics simulations. These magnitudes are about one order of magnitude lower than those reported by Zhang et al. [61] for sodium silicate glasses and the experimental roughness of polished glass surfaces (0.1–1.5 nm) [62,63]. The difference arises primarily from the limited lateral dimensions of the simulated systems and the surface preparation procedure adopted here—surfaces were created by melting after cutting along *z* rather than by fracturing—which suppresses the long-wavelength height fluctuations captured in experiments and larger-scale MD models [37,64].

Upon densification at 1.5 GPa, both glass compositions exhibit a clear reduction in roughness, but the magnitude of the decrease depends on composition. In the sodium aluminosilicate (AL) glass, R_a decreases from 0.208 nm to 0.194 nm, and R_q from 0.277 nm to 0.261 nm (≈ 6 % reduction), indicating that pressure produces a more uniform and compact surface. For the sodium silicate (NS) glass, the reduction is slightly larger (≈ 9 %), with R_a decreasing from 0.238 nm to 0.217 nm and R_q from 0.317 nm to 0.289 nm. The three roughness descriptors (R_a, R_q, σ_{hmax}) provide consistent trends, confirming that densification smooths the surface topography.

At both densities, the NS glass exhibits higher roughness than the AL glass: R_a, R_q, and σ_{hmax} values are roughly 15–20 % larger. This compositional dependence reflects the structural role of sodium. In NS, sodium acts as a network modifier, generating non-bridging oxygens (NBOs) that break Si–O–Si linkages and increase local height fluctuations. In contrast, in AL glass sodium behaves mainly as a charge compensator for $[AlO_4]^-$ tetrahedra, preserving network connectivity and producing intrinsically smoother surfaces even before densification.

3.2. Indentation tests

3.2.1. Load displacement curves and hardness

Fig. 5 presents the simulated load–displacement (P–h) curves for the sodium aluminosilicate (AL) and sodium silicate (NS) glasses, both in their pristine and pre-densified (1.5 GPa) states, while Table 3 summarizes the corresponding indentation parameters obtained through the Oliver–Pharr (OP) analysis as well as the hardness estimates obtained using the alternatic geometric approach described in the computational section and denoted as H_{cone}.

All curves display the typical elastic–plastic response observed during indentation of silicate glasses, [11,31,65] a smooth loading non-linear segment followed by a drop in force at the maximum indentation depth ascribed to stress relaxation during the holding stage and an unloading branch whose slope reflects the elastic recovery of the material. The maximum load (P_{max}), indentation depths (h_{max}, h_f, h_c) and calculated hardness values highlight clear compositional and pressure-induced effects.

For both compositions, the application of a pre-densification treatment at a pressure of 1.5 GPa leads to a noticeable increase in stiffness and maximum load, together with a reduction in penetration depth. In

Table 3
Maximum load (P_{max}), maximum indentation depth (h_{max}), residual depth after unloading (h_f), contact depth (h_c), and hardness (H) obtained from the Oliver–Pharr analysis (OP) or using the lateral cone area (Eq. (14)) for pristine and pre-densified sodium aluminosilicate (AL) and sodium silicate (NS) glasses. Hardness values were computed from the simulated load–displacement curves reported in Fig. 2 using Eq. (10)-(13) and compared with available experimental data (H_{exp}) from Refs. [66,67]. All quantities are in Å or GPa, and the pressure applied during densification is given in GPa after each composition label (e.g., AL 1.5 = AL glass pre-densified at 1.5 GPa).

	P_{max} (eV/Å)	h_{max} (Å)	h_f (Å)	h_c (Å)	H_{OP} (GPa)	$H_{cone.}$ (GPa)	$H_{exp.}$ (GPa)
AL	323.0	47.0	36.0	42.9	14.0	13.3	7.5 [66]
AL 1.5	339.0	44.5	34.0	40.0	16.8	15.6	\
NS	259.6	45.0	36.0	41.8	11.9	10.7	7.2 [67]
NS 1.5	320.2	45.5	35.0	41.4	14.9	13.9	\

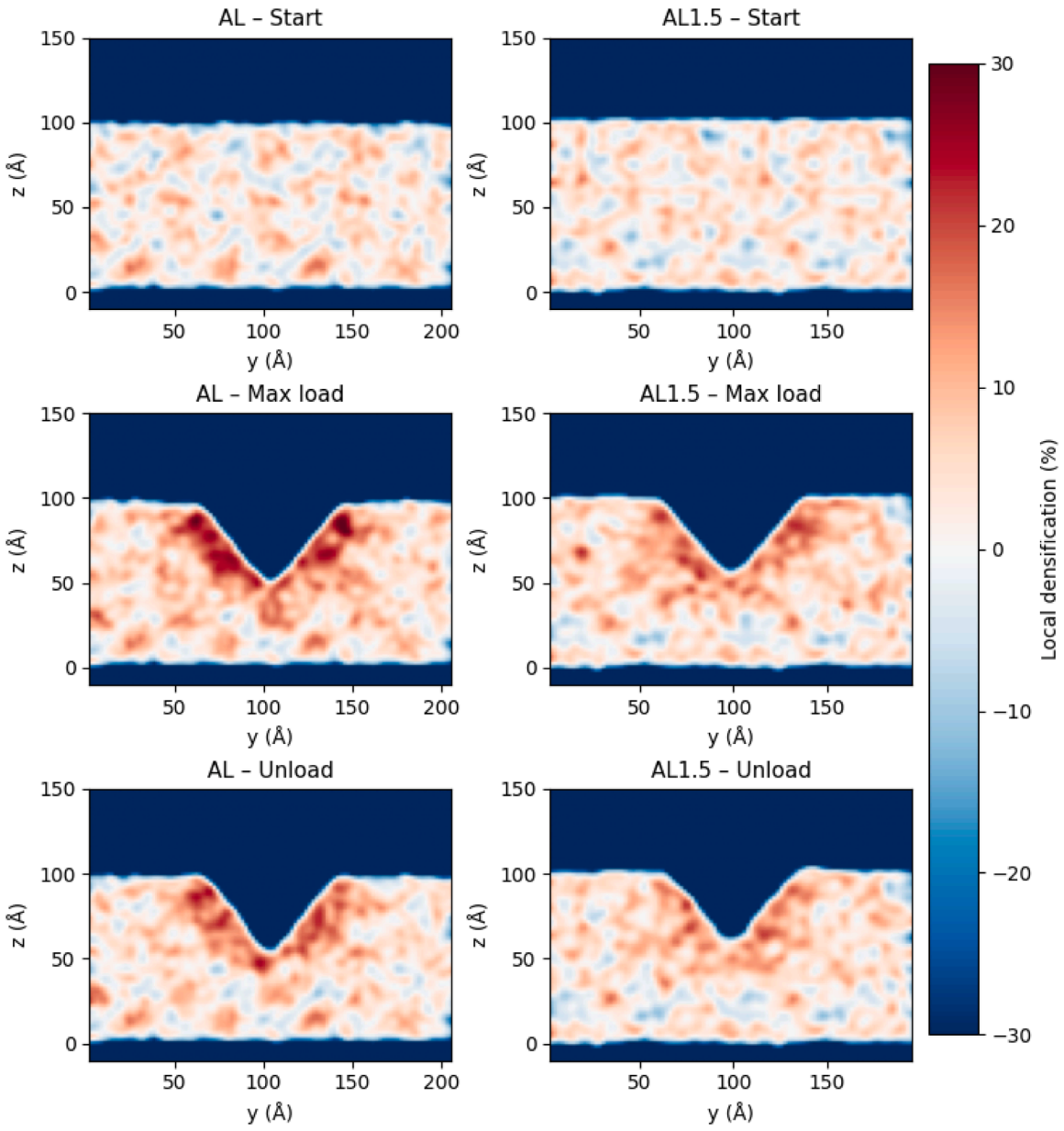

Fig. 6. Local densification maps for the aluminosilicate glasses: pristine AL (left column) and pre-densified AL 1.5 (right column). Rows correspond to the initial state, maximum load, and after unloading. Maps were generated from the LAMMPS outputs by binning the box with a 2 × 2 × 2 Å^3 grid and extracting a y–z slice centred at $x = L_x/2$ with 12 Å thickness. For each bin the local density was compared to the composition-specific bulk density before indentation and reported as densification $\Delta\rho/\rho_0 \times 100$. The gridded fields were lightly smoothed (Gaussian $\sigma = 1.5$ bins). The colour scale is fixed to [−30 %, +30 %] and centred at 0. Pristine AL shows a larger and deeper densified zone beneath the tip, whereas AL 1.5—already compact—exhibits a more confined densification pattern during loading and after unloading. The blue regions into the panels surrounding the slab models represent void region into the simulation box, not a negative densification. The value ranges of the colormap was chosen based on the maximum positive local densification value observed and then a symmetric colormap was created.

the AL glass, P_{max} rises from 323 to 339 eV Å^{-1}, h_{max} decreases from 47 to 44.5 Å, and hardness computed with the OP method increases from 14.0 to 16.8 GPa. A similar trend is observed for NS, where P_{max} grows significantly from 259.6 to 320.2 eV Å^{-1} and hardness from 11.9 to 14.9 GPa.

The hardness values obtained using the cone-based contact area (H_{cone}) follow the same trends as the OP hardness but presenting slightly lower values (of about 1 GPa). This consistency confirms that the observed trends are robust and not an artefact of the specific contact-area definition.

The reduction in residual depth (h_f) and in h_c in pre-densified glasses reflects their reduced propensity for irreversible densification and thus a higher degree of reversible (elastic-like) recovery upon unloading. This behavior is consistent with experimental observations showing that pressure-treated silicates exhibit increased stiffness and a diminished capacity for further compaction [9,10,65].

When comparing the two compositions, NS glasses exhibit systematically lower maximum loads and hardness than their aluminosilicate counterparts, reflecting the structural role of sodium. In NS, Na acts as a network modifier, breaking Si–O–Si linkages and producing non-bridging oxygens that weaken the network connectivity. The resulting open structure facilitates plastic deformation during indentation, producing softer, more compliant surfaces with larger residual depths. In contrast, in the AL glass sodium primarily serves as a charge compensator for $[AlO_4]^-$ tetrahedra, maintaining a highly interconnected and compact framework and yielding higher stiffness and hardness.

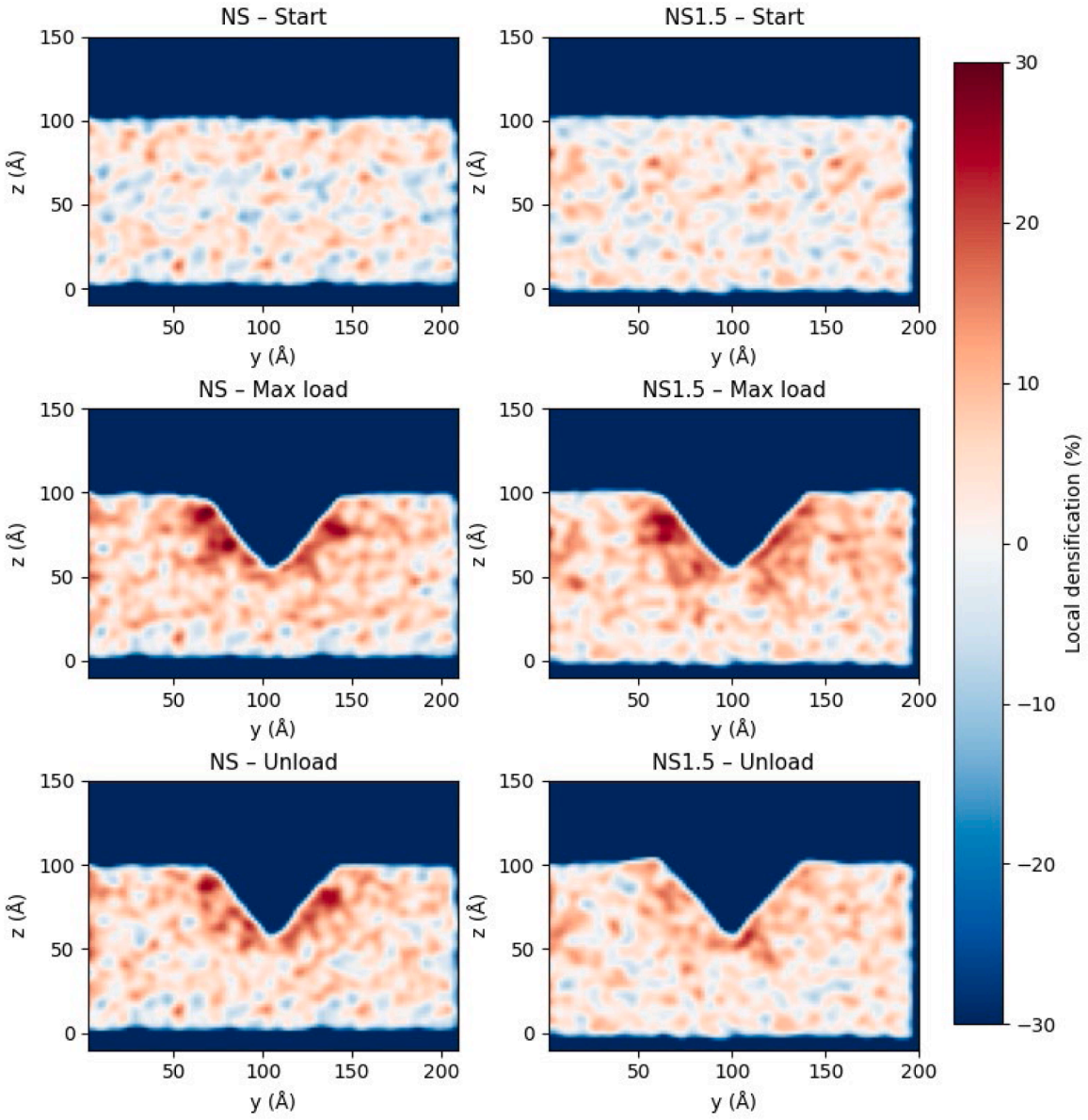

Fig. 7. Local densification maps for the sodium silicate glasses: pristine NS (left column) and pre-densified NS 1.5 (right column). Rows show initial, maximum load, and unloaded configurations. Processing matches Fig. 6: chunk/atom bin/3d with 2 × 2 × 2 Å³ bins, mid-x slice of 12 Å thickness, densification computed relative to each composition's pre-indentation bulk density (ρ_0), Gaussian smoothing ($\sigma = 1.5$ bins), and a fixed [−30 %, +30 %] color range centered at 0. As in AL, pristine NS exhibits a broader densified region under the indenter, while NS 1.5 shows more localized compaction due to its reduced capacity for further densification. The blue regions into the panels surrounding the slab models represent void region into the simulation box, not a negative densification. The value ranges of the colormap was chosen based on the maximum positive local densification value observed and then a symmetric colormap was created.

Pre-densification enhances packing of the network and increasing connectivity, thereby strengthening both compositions. As a result, charge-balanced aluminosilicates exhibit higher P_{max} and H, while depolymerized sodium silicates remain more deformable and thus softer.

In conclusion of this section, we would like to highlight that albeit the cone-based hardness values are systematically lower than those obtained using the Oliver–Pharr method, the quantitative improvement remains moderate, and the calculated hardness values are still consistently higher than experimental data. This indicates that, while the cone-based approach provides a conservative and atomistically grounded estimate that mitigates some limitations of continuum contact mechanics at the angstrom length scale, the remaining discrepancy is likely dominated by the intrinsic stiffness of the empirical interatomic potential under the extreme local stresses generated during indentation.

3.2.2. *Local density, stress and strain distributions*

Figs. 6 and 7 show the evolution of local densification around the indenter during the loading and unloading stages for the AL and NS glass families, respectively. Each figure compares the pristine compositions (left panels) with their pre-densified counterparts treated at 1.5 GPa (right panels). The three rows correspond to the initial configuration, the maximum indentation load, and the post-unloading state. The top panels in each figure also report the local density before indentation to provide a direct reference for the changes in compactness during the indentation cycle.

The local densification was calculated using the chunk/atom bin/3d command in LAMMPS with a 2 × 2 × 2 Å³ grid. For each bin, the local density during indentation was compared to the bulk density of the same glass prior to indentation, and the relative change was expressed as a percentage. Positive values (red) indicate local compaction of the glass

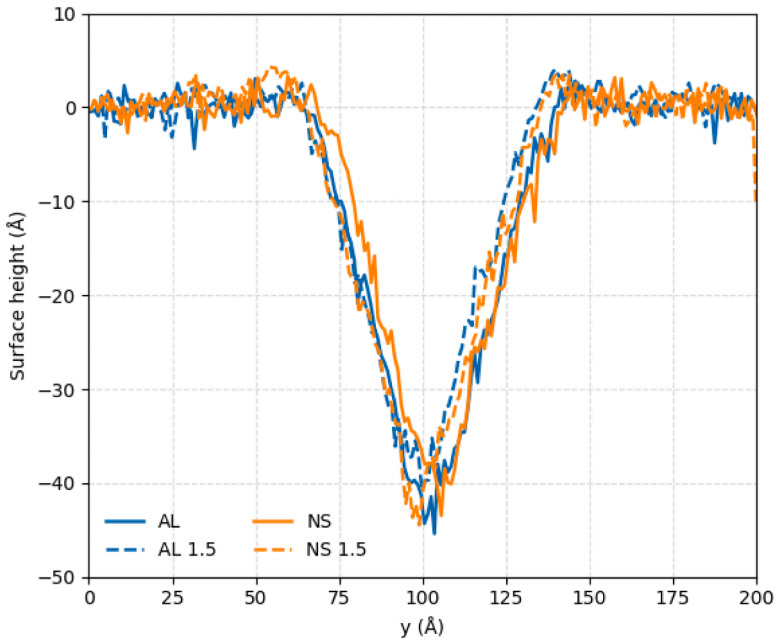

Fig. 8. Average z-profile of the post-indentation glass surfaces obtained from the atomic configurations after unloading. The surface trace was computed by dividing the simulation cell into bins of 1 Å along the y direction within an yz slice centered at mid-x (±6 Å thickness). For each bin, the outermost atomic position (z_{max}) of the glass atoms (Na, Si, Al, O) was extracted, excluding the carbon atoms of the indenter. The resulting profiles represent the average surface height after indentation for the pristine and pre-densified glasses. The pre-densified samples (AL 1.5 and NS 1.5) display a small pile-up of material of about 5 Å at the edge of the indent, consistent with strain relaxation and plastic shear in the already densified networks.

network. Apparent negative values (blue) do not represent physical dilatation of the glass; instead, they arise from bins located in the vacuum regions of the simulation box surrounding the free-standing slab, where the local density is close to zero. These regions are included in the spatial binning for technical reasons related to the construction of the density maps and should be interpreted solely as empty space, not as negative densification of the material.

During loading, all glasses develop a strongly densified zone under the tip, consistent with the compressive stresses generated at the contact. However, the extent and magnitude of this densification depend on both composition and pre-densification. In the pristine glasses, the densified region is larger and extends deeper, reflecting their higher free volume and greater compressibility. In contrast, the pre-densified AL 1.5 and NS 1.5 samples show a smaller, shallower densified region, as their initially compact structures limit further densification. This trend correlates with the higher hardness and reduced penetration depth measured for the pre-densified systems.

After unloading, partial elastic recovery occurs, but the densified zones persist beneath the residual imprint. Notably, the pre-densified glasses exhibit a slight pile-up of material (≈ 5 Å) at the rim of the indentation, as highlighted in Fig. 8. This pile-up originates from strain relaxation dominated by plastic shear, since further volumetric compaction is hindered by the already high network density. Consequently, while pristine glasses deform primarily by densification, pre-densified ones accommodate deformation mainly through lateral flow, producing the observed surface uplift at the indent boundary.

To obtain an atomistically resolved picture of the volumetric changes occurring during indentation, we also evaluated the variation of the atomic Voronoi volume for each configuration along the loading–unloading cycle. The resulting ΔV maps, reported in Fig. 9, provide a direct measure of local free-volume collapse or expansion at the single-atom level. In all glasses, a pronounced reduction of Voronoi volume develops beneath the indenter at maximum load, consistent with the densified regions identified in the binned density fields. However, the extent and permanence of this volume collapse depend strongly on composition and on the initial degree of compaction. Pristine NS and AL glasses display a broader and deeper $\Delta V < 0$ zone with respect to pre-densified glasses, which exhibit a more confined reduction of atomic volume and a greater degree of recovery after unloading. Moreover, small regions with $\Delta V > 0$ emerge near the edge of the indent in the pre-densified samples, indicating localized dilatation associated with lateral material flow. These atomic-scale free-volume variations provide a complementary and highly resolved view of densification and its interplay with shear-mediated deformation during the indentation process.

It is worth to note that, the magnitude of residual densification observed in our simulations (typically 8–15 % depending on composition, and exceeding 20–30 % in the most compressed local regions beneath the indenter at maximum loading) is consistent with Raman- and Brillouin-based experimental characterizations of indentation-induced densification in oxide glasses. Experimental studies by Rouxel et al. [14], Winterstein-Beckmann et al. [15], Ji et al. [10], and Vandembroucq et al. [68] report residual densification values between ~5 % and ~20 % depending on glass composition, network connectivity, and measurement depth, with localized densification zones reaching even higher values. Although experimental characterisation lacks atomistic resolution, the amplitude and spatial confinement of the densified region beneath the indent agree well with our atomistic predictions.

Figs. 10–12 present the evolution of local shear stress, shear strain, and non-affine atomic displacements (D^2_{min}) [69] around the indenter for the four glass compositions (AL, AL 1.5, NS, NS 1.5) at maximum load and after unloading. Each row compares the different glass families, while the two columns correspond to the maximum loading and post loading stages. All quantities were evaluated on an *yz* slice at middle x position of the box size (x-mid) as done for Fig. 6 and 7.

These maps present complementary insights into the mechanism of plastic deformation during indentation.

Local shear stresses (Fig. 10) were obtained from the per-bin virial tensors computed in LAMMPS via `compute stress/atom` command and spatially averaged using `fix ave/chunk` with a $2 \times 2 \times 2$ Å^3 bin size [70]. The virial stresses were converted to GPa and smoothed with a Gaussian kernel to highlight mesoscale variations.

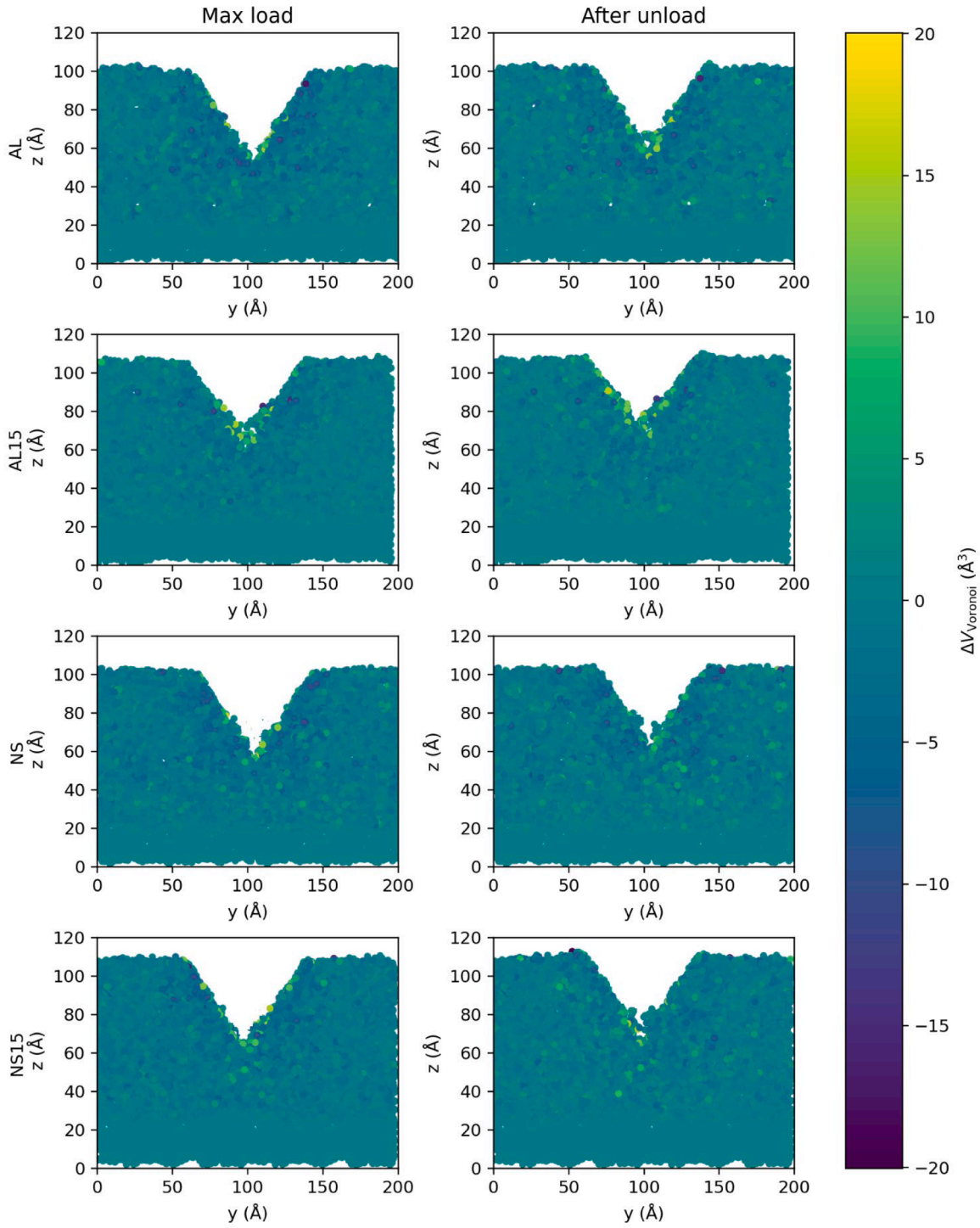

Fig. 9. Voronoi atomic-volume variations (ΔV) for all glass compositions at maximum load and after unloading. Maps represent the change in atomic Voronoi volume relative to the undeformed slab ($\Delta V = V(t) - V_0$), projected onto a y–z slice at mid-x (±6 Å thickness). Negative values (blue) indicate local free-volume collapse (densification), whereas positive values (red) correspond to local dilatation. For each composition (rows: AL, AL 1.5, NS, NS 1.5), the left column shows the configuration at maximum indentation load and the right column the configuration after unloading. Pristine glasses exhibit broad and persistent zones of negative ΔV beneath the indenter, consistent with irreversible densification, while pre-densified glasses show more confined compaction and the emergence of positive ΔV regions near the indent boundary, associated with shear-mediated lateral flow. The colour scale is fixed across all panels to facilitate quantitative comparison.

Because the imprinting load is applied along the z direction, we focus on the σ_{yz} component of the stress tensor, which directly captures shear transfer within the analysed yz plane. This component is particularly sensitive to localized plastic rearrangements driven by gradients in the axial stress σ_{zz} beneath the imprint. Although scalar invariants such as the von Mises stress were also evaluated, they combine axial and shear contributions and were found to provide less direct insight into the directional nature of stress relaxation in the present geometry.

The maps reveal intense σ_{yz} lobes beneath the tip at maximum load, indicating regions of opposite shear. These stress fields persist after unloading, confirming that permanent shear offsets remain even after elastic recovery. The overall stress magnitudes are comparable across

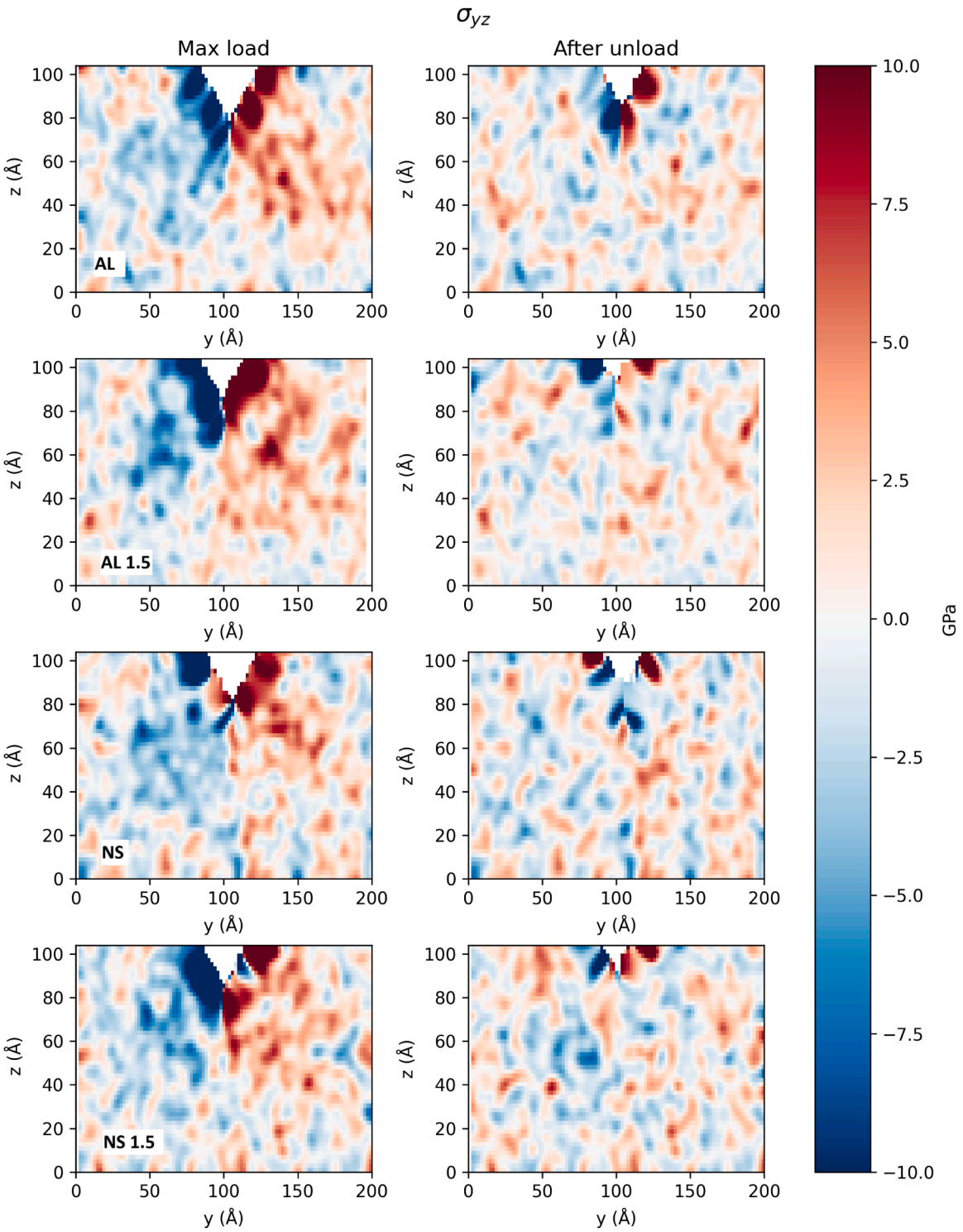

Fig. 10. Shear stress maps (σ_{yz}, in GPa) on the yz slice at mid-x (*±6 Å thickness*) for four glass compositions (rows: AL, AL1.5, NS, NS1.5) at two indentation states (columns: Max load and After unload). Bin-resolved virial stresses were computed from LAMMPS *ave/chunk* outputs, converted to GPa assuming a bin volume of dx·dy·dz, and smoothed with a Gaussian filter (σ = 1.5 pixels). For visualization, z coordinates were shifted so that the minimum z in each panel corresponds to 0 Å. Colour limits were set to ±10 GPa for σ_{yz} unless otherwise noted.

compositions, but the stress distribution becomes more diffuse in the pre-densified glasses, where shear is accommodated over a broader area near the surface, consistent with the pile-up observed in Figs. 6 and 7.

The corresponding local shear strain maps (Fig. 10) were calculated from atomistic configurations by least-squares fitting the local deformation gradient **F** to the displacements of neighbouring atoms within a 5 Å cut-off, enforcing periodic boundary conditions and the minimum-image convention. The symmetric strain tensor $\mathbf{e} = \frac{1}{2}(\mathbf{F} + \mathbf{F}^{T}) - \mathbf{I}$ was used to extract the e_{yz} component.

These maps represent the affine (elastic) part of the atomic deformation. In all glasses the strain patterns closely follow the stress fields, showing localized regions of high e_{yz} beneath the indenter. However, the magnitude and spatial extend of the affine shear strain are similar across all compositions, suggesting that elastic and reversible part of the

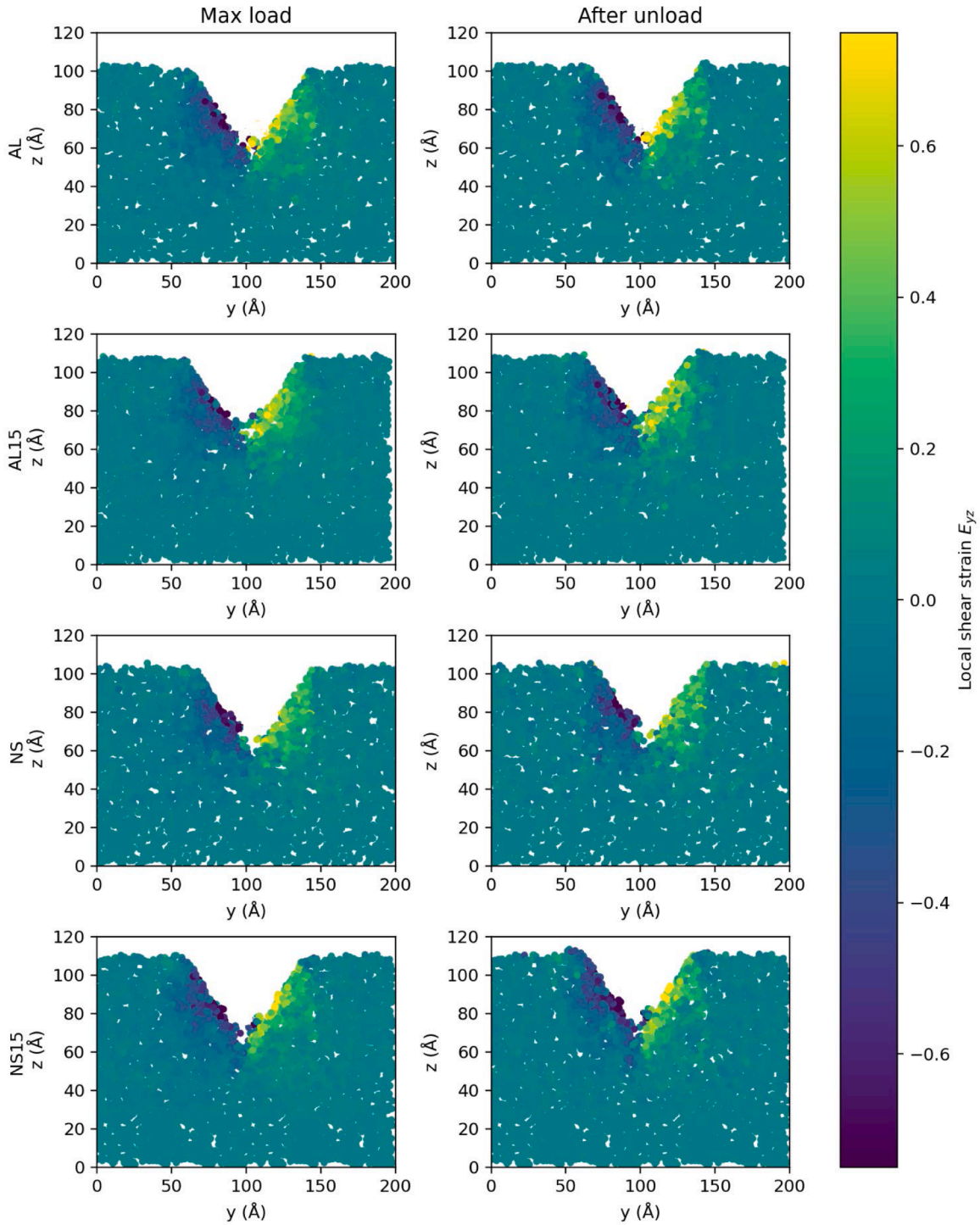

Fig. 11. Local shear strain maps (e_{yz}) on the yz slice at x-mid (±3 Å thickness) for AL, AL1.5, NS, and NS1.5 glasses (rows) at Max load and After unload (columns). The local deformation gradient F was estimated per atom via least-squares over neighbours within r_{cut} = 5 Å and up to a maximum of 40 neighbours, enforcing periodic boundary conditions and the minimum-image convention. The small-strain tensor $E = \frac{1}{2}(F + F^T) - I$ was used to extract e_{yz}. Deformed coordinates were used for plotting to reveal the indentation cavity; common colour limits were fixed to [−0.75, 0.75] for comparability. z coordinates were shifted so that the minimum z in each panel corresponds to 0 Å.

deformation is comparable, regardless of pre-densification. This confirms that the structural stiffening induced by pre-densification primarily affects the plastic, rather than the elastic response.

Finally, the D^2_{min} maps (Fig. 12) quantify the non-affine atomic displacements, computed as the mean-squared deviation of each atom's local neighbourhood from the best affine transformation fitted to its reference configuration. D^2_{min} therefore isolates irreversible, non-elastic rearrangements and provides a direct measure of plastic activity independent of the elastic strain. The bright yellow regions beneath the tip correspond to atoms undergoing large non-affine motions during indentation, outlining the shear transformation zones responsible for plastic flow. The D^2_{min} maps show that plastic activity is more spatially extended in the pre-densified glasses than in the pristine ones, even though their local densification is reduced. This indicates a shift in the

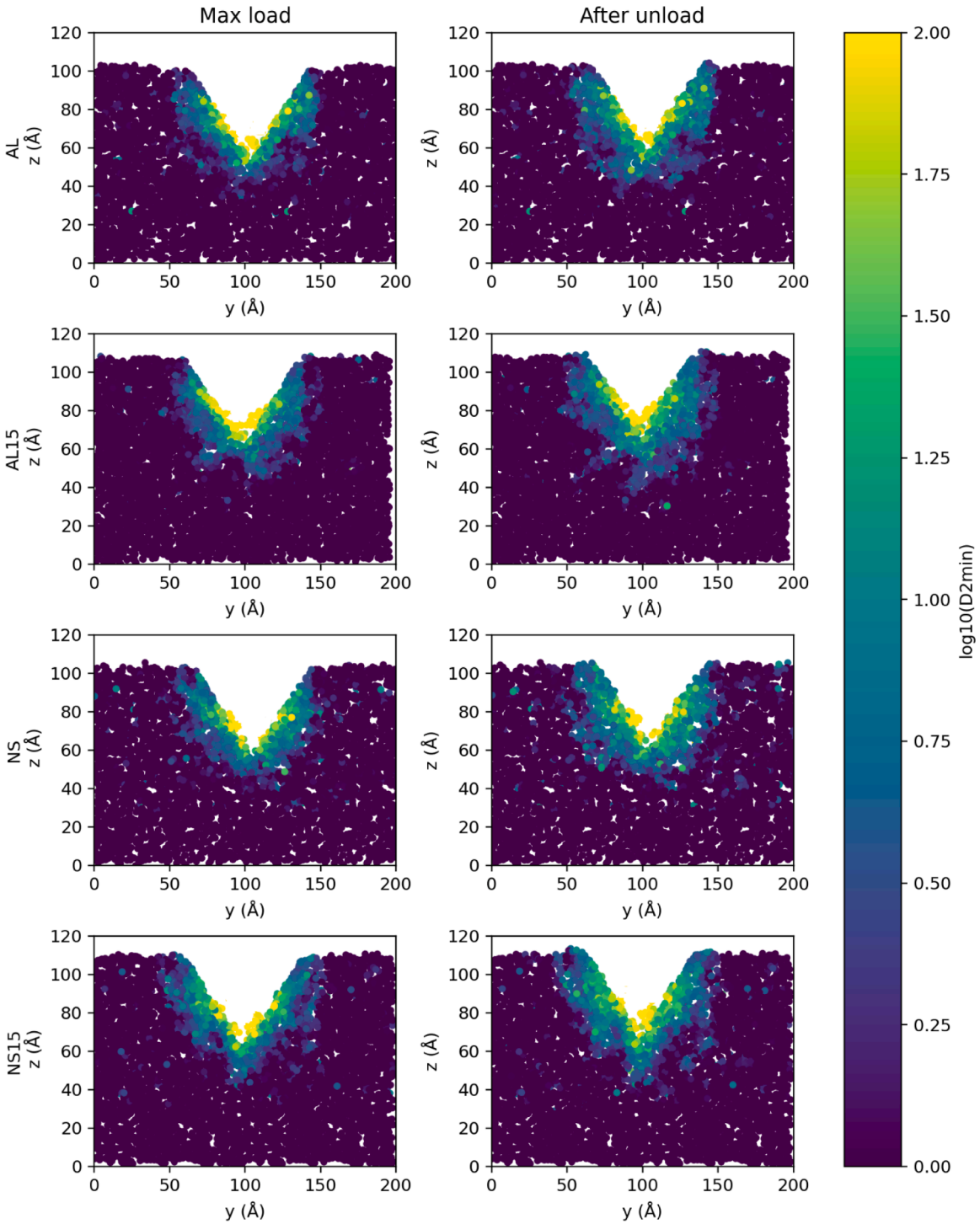

Fig. 12. Non-affine displacement maps (D^2_{min}) on the yz slice at x-mid (±3 Å thickness) for AL, AL15, NS, and NS15 glasses (rows) at Max load and After unload (columns). For each atom, D^2_{min} was computed as the mean squared residual $\|r' - F\,r\|^2$ across its neighbour shell after fitting the best local affine transformation F (PBC + minimum image). Values are shown as $\log_{10}(D^2_{min})$ with a global colour range (from 0 to $\log_{10}\max(D^2_{min})$) across all systems and states. Deformed coordinates were used for plotting; z coordinates were shifted so that the minimum z in each panel corresponds to 0 Å.

dominant plastic mechanism: pristine AL and NS glasses deform mainly by local densification beneath the indenter, while pre-densified AL 1.5 and NS 1.5 glasses, having limited capacity for further compaction, accommodate plasticity through shear flow. The broad, high-D^2_{min} regions in these glasses reflect collective non-affine rearrangements associated with shear-dominated flow, which is also responsible for the observed surface pile-up after unloading. Overall, these results confirm that pre-densification suppresses volumetric compaction but enhances shear-mediated plastic deformation, marking a transition from densification-driven to shear-flow-driven plasticity.

The observed transition from densification-dominated plasticity in pristine NS to shear-mediated deformation in AL and in the pre-densified glasses is fully consistent with experimental observations. Raman mapping and indentation studies [14,27,65] show that more polymerized or pre-densified networks exhibit reduced densification and a more prominent contribution from shear flow. Similarly, mechanical and

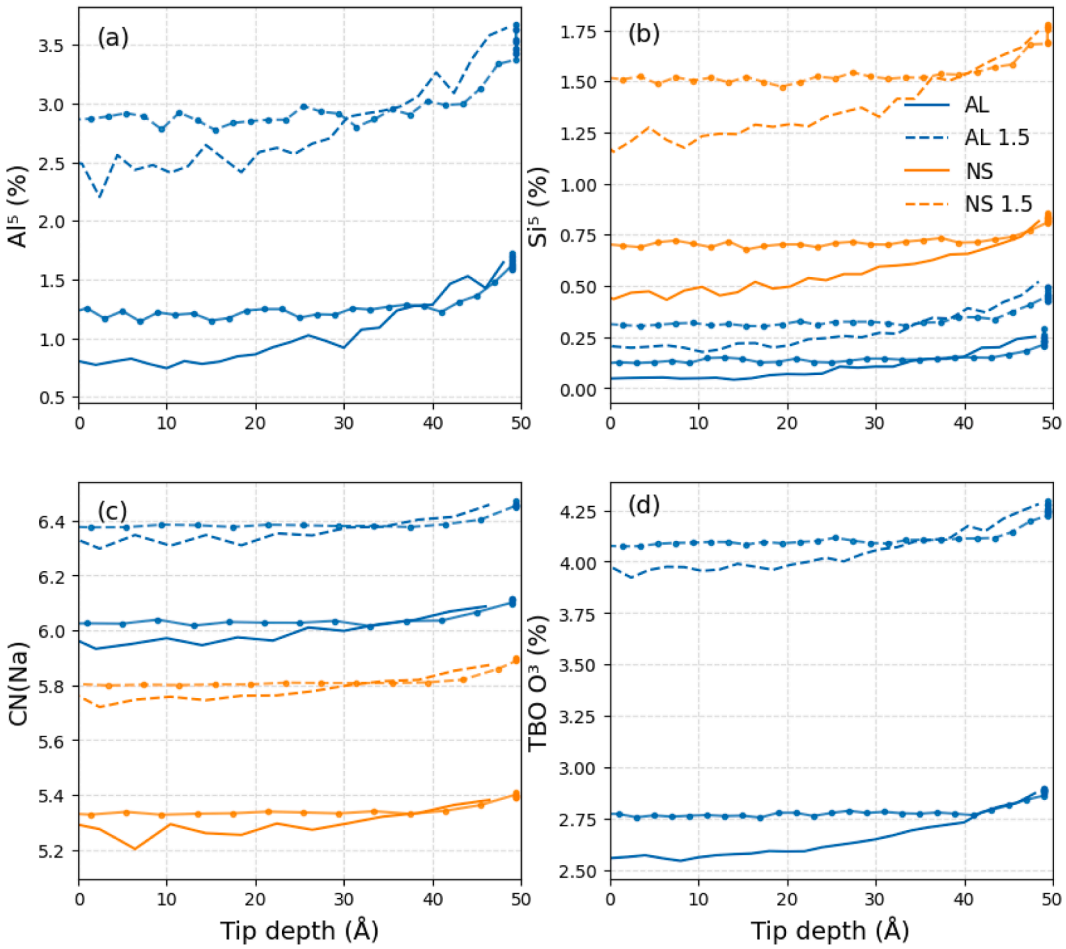

Fig. 13. Evolution of the (a) Al[5], (b) Si[5], (c) average CN of Na $\langle CN_{Na} \rangle$, (d) TBO for all the investigated glasses during loading and unloading (circles).

spectroscopic measurements on aluminosilicate glasses [71] identify increased shear accommodation in compositions with higher angular flexibility, that is, the ability of O–T–O and T–O–T bond angles (T = Si or Al) to bend under stress without breaking bonds.

3.2.3. *Structural variations around the tip: the coordination numbers*

Figs. 13 and 14 provide a detailed picture of how the local glass structure responds to indentation, both during loading and after unloading. Fig. 13 reports the evolution of the population of over-coordinated species—namely Al[5] (panel a), Si[5] (panel b), the average coordination number of Na (CN(Na)) (panel c), and three-bridging oxygens (TBOs, panel d)—as a function of the penetration depth of the indenter. For the aluminosilicate glasses (AL and AL 1.5), Al[5] increases steadily during loading, reaching about 1.6 % in the pristine glass and 3.5 % in the pre-densified sample at maximum penetration. Upon unloading, these values decrease but do not fully return to their initial levels, indicating a partially reversible transformation. Si over-coordination in AL glasses remains extremely low throughout loading and unloading, suggesting that Si–O tetrahedra are not the primary structural units accommodating deformation. Na shows a systematic increase in coordination during loading and a near-complete recovery upon unloading, reflecting the high mobility and structural adaptability of Na^+ in the network. TBOs follow the same qualitative trend as Al[5], appearing only in the AL compositions, with slightly higher values in the pre-densified glass; their evolution is modest but again partly reversible.

These coordination changes are also consistent with experimental high-pressure NMR and EXAFS measurements. For example, Allwardt & Stebbins [6], Kelsey et al. [72], and Bista & Stebbins [17] report the appearance of Si^5, Al^5, and Al^6 species in compressed aluminosilicate and sodium aluminosilicate glasses at pressures comparable to those reached locally beneath a sharp indenter. While such measurements cannot be performed in situ during indentation, the types of coordination defects observed experimentally under hydrostatic compression closely match those that emerge in our simulations during localized contact loading.

The sodium silicate glasses (NS and NS 1.5) present a different scenario. These glasses exhibit a higher initial concentration of Si[5], which further grows during loading and remains elevated after unloading. Importantly, no TBOs form in NS glasses, and the Si[5] population shows limited reversibility, indicating a more persistent structural modification. Na coordination changes in NS are similar to AL, although the coordination number is lower because of the modifying role of Na in the NS glasses. Together, these trends reveal a clear compositional dependence: AL glasses accommodate deformation primarily through changes in Al and Na coordination, while NS glasses respond predominantly through Si-centered network compaction and Na coordination changes.

Fig. 14 complements these global trends by showing the spatial distribution of atoms that experience a coordination increase ≥ 1 relative to the initial state. For NS glasses, Si atoms with increased coordination are highly localized beneath the indent and within the pile-up region, consistent with a densification-dominated response concentrated near the indenter. In AL glasses, however, Al atoms with increased coordination are distributed more broadly around the tip, and Na atoms with increased CN appear throughout the deforming volume. This widespread spatial distribution of Na and Al defects is characteristic of deformation governed by shear flow and non-affine rearrangements rather than purely volumetric compaction.

Taken together, these results show that the hierarchy of structural

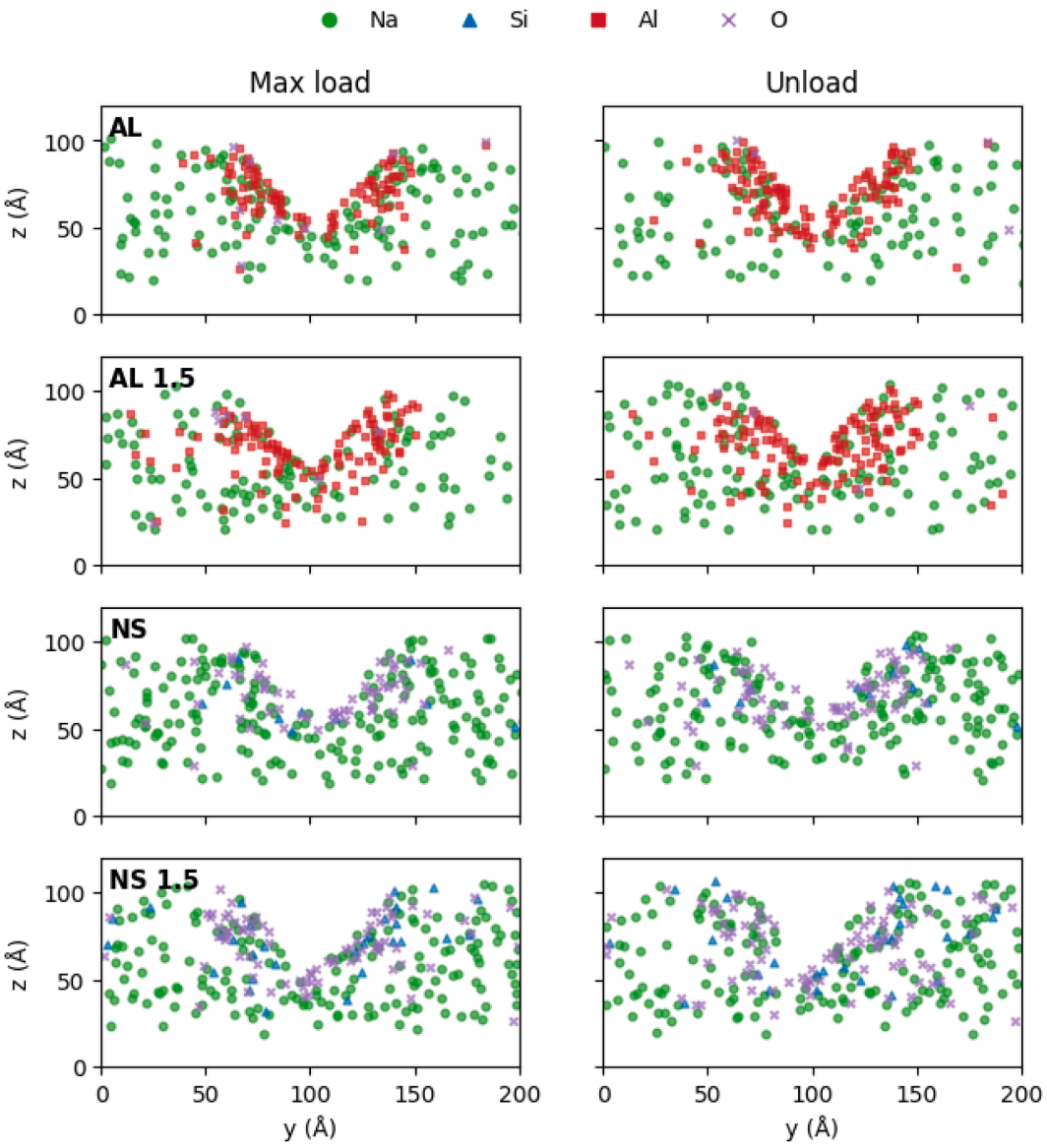

Fig. 14. Spatial distribution of the atoms that have increased their coordination number at the maximum loading depth (load max) and after unloading (unloaded), with respect to the initial undeformed state.

flexibility in the glasses is Na > Al > Si, and that the dominant deformation mechanism shifts according to composition and pre-densification. In pristine NS glasses, indentation induces persistent Si over-coordination and localized densification, in agreement with prior nanoindentation experiments and Raman/Brillouin studies that reveal persistent densified zones beneath indent imprints in silica and soda-lime silicate glasses [15,68,73]. In contrast, AL and pressure-densified glasses exhibit a more shear-dominated response, with deformation accommodated by reversible Al[5]/TBO formation and significant Na rearrangement, consistent with experimental findings on compressed aluminosilicates showing enhanced shear flow, reduced densification, and increased populations of high-coordination Al species [8,71,72]. Molecular dynamics simulations on silicate and aluminosilicate systems have similarly reported that (i) Na coordination responds in a highly reversible manner, (ii) Al acts as a deformation-active network former while Si remains comparatively rigid, and (iii) increased polymerization suppresses densification and enhances shear-controlled deformation [11,31,57].

In summary, Figs. 13 and 14 demonstrate that indentation induces substantial structural rearrangements whose magnitude and reversibility depend on composition. AL and pre-densified glasses deform primarily through shear-mediated bond rearrangements involving Al and Na, while NS glasses respond through more permanent densification of the Si-O network. These insights strengthen the mechanistic interpretation presented in the previous sections: deformation in sodium-containing oxide glasses results from competing densification and shear-flow pathways, with their balance governed by the roles and mobility of Na, Al, and Si within the network.

4. Conclusions

This work demonstrates that glass composition and pressure history dictate the balance between densification and shear flow, the two fundamental pathways governing plastic deformation during nanoindentation. By systematically comparing pristine and pre-densified sodium silicate (NS) and sodium aluminosilicate (AL) glasses, we reveal a clear hierarchy of structural flexibility—Na > Al > Si—and its consequences for hardness, defect formation, and residual imprint morphology.

In pristine NS glasses, plasticity is dominated by irreversible

densification, accompanied by persistent Si over-coordination and a compacted zone localized beneath the indenter. NS exhibits the largest penetration depth and lowest hardness because its open, highly depolymerized network—rich in non-bridging oxygens and Na modifiers—offers a low-energy pathway for volume collapse. Thus, even though NS deforms primarily through densification, this mechanism is easier than the shear-mediated rearrangements available in more connected networks, explaining why NS is mechanically softer.

In contrast, AL glasses are less inclined to densification and instead deform more through shear flow, mediated by reversible coordination changes of Al (Al[5] and TBO formation) and extensive Na rearrangement. The stronger Si–O–Al connectivity and reduced NBO content make volume collapse energetically costly, so plasticity proceeds predominantly via non-affine shear and bond switching. These shear-dominated pathways are mechanically harder to activate, yielding higher hardness and smaller residual densification. This difference in accessible deformation modes explains why AL is harder than NS despite relying on shear rather than densification.

Pre-densification suppresses additional densification in both compositions by reducing free volume and increasing network connectivity. As a result, plasticity in densified NS and AL glasses is forced to proceed mainly through shear-assisted atomic rearrangements, which manifest as broad non-affine displacement fields and—as observed in AL—small pile-ups at the indentation rim. These features indicate a shift from densification-dominated to shear-dominated plasticity as densification capacity is exhausted.

The spatial distribution of atoms with increased coordination further reinforces this mechanistic picture. In NS, Si with altered coordination is concentrated beneath the imprint, consistent with densification-driven deformation. In AL, Al and Na with increased coordination are spread over a larger region around the indenter, demonstrating the more delocalized nature of shear flow. Na, in particular, responds in a highly reversible and spatially extended manner, confirming its role as the most flexible structural species.

Altogether, these findings integrate and extend previous experimental and computational studies on indentation-induced densification and shear flow in oxide glasses. They clarify how network chemistry (Si vs Al) and modifier content (Na) determine the preferred deformation mode, and how pressure history can tune the mechanical response by shifting the accessible deformation pathways. These mechanistic insights provide a foundation for designing silicate glasses with tailored resistance to contact damage, optimized hardness, and controlled plasticity through precise adjustment of composition and processing conditions.

CRediT authorship contribution statement

Alfonso Pedone: Conceptualization, Investigation, Formal analysis, Data curation, Writing – original draft. **Annalisa Pallini:** Investigation. **Leopold Talirz:** Writing – review & editing. **Wolfgang Mannstadt:** Writing – review & editing.

Declaration of competing interest

The authors declare that they have no known competing financial interests or personal relationships that could have appeared to influence the work reported in this paper.

Acknowledgements

SCHOTT AG. and the department of Chemical and Geological Sciences of the University of Modena and Reggio Emilia are acknowledged for the partial financing of the PhD scholarship of Annalisa Pallini.

Supplementary materials

Supplementary material associated with this article can be found, in the online version, at doi:10.1016/j.jnoncrysol.2026.124105.

References

[1] A.R. Boccaccini, Machinability and brittleness of glass-ceramics, J. Mater. Process. Technol. 65 (1997) 302–304, https://doi.org/10.1016/S0924-0136(96)02275-3.
[2] J. Sehgal, S. Ito, Brittleness of glass, J. Non-Cryst. Solids 253 (1999) 126–132, https://doi.org/10.1016/S0022-3093(99)00348-8.
[3] A.K. Varshneya, Fundamentals of Inorganic Glasses, Gulf Professional Publishing, 1994.
[4] E.D. Zanotto, J.C. Mauro, The glassy state of matter: its definition and ultimate fate, J. Non-Cryst. Solids 471 (2017) 490–495, https://doi.org/10.1016/j.jnoncrysol.2017.05.019.
[5] M.N. Svenson, T.K. Bechgaard, S.D. Fuglsang, R.H. Pedersen, A.Ø. Tjell, M. B. Østergaard, R.E. Youngman, J.C. Mauro, S.J. Rzoska, M. Bockowski, M. M. Smedskjaer, Composition-structure-property relations of compressed borosilicate glasses, Phys. Rev. Appl. 2 (2014) 024006, https://doi.org/10.1103/PhysRevApplied.2.024006.
[6] J.R. Allwardt, J.F. Stebbins, B.C. Schmidt, D.J. Frost, A.C. Withers, M. M. Hirschmann, Aluminum coordination and the densification of high-pressure aluminosilicate glasses, Am. Mineral. 90 (2005) 1218–1222, https://doi.org/10.2138/am.2005.1836.
[7] M. Grimsditch, A. Polian, A.C. Wright, Irreversible structural changes in vitreous ${\mathrm{B}}_{2}$${\mathrm{O}}_{3}$ under pressure, Phys. Rev. B 54 (1996) 152–155, https://doi.org/10.1103/PhysRevB.54.152.
[8] T.K. Bechgaard, A. Goel, R.E. Youngman, J.C. Mauro, S.J. Rzoska, M. Bockowski, L. R. Jensen, M.M. Smedskjaer, Structure and mechanical properties of compressed sodium aluminosilicate glasses: role of non-bridging oxygens, J. Non-Cryst. Solids 441 (2016) 49–57, https://doi.org/10.1016/j.jnoncrysol.2016.03.011.
[9] S. Kapoor, L. Wondraczek, M.M. Smedskjaer, Pressure-induced densification of oxide glasses at the glass transition, Front. Mater. 4 (2017), https://doi.org/10.3389/fmats.2017.00001.
[10] H. Ji, V. Keryvin, T. Rouxel, T. Hammouda, Densification of window glass under very high pressure and its relevance to Vickers indentation, Scr. Mater. 55 (2006) 1159–1162, https://doi.org/10.1016/j.scriptamat.2006.08.038.
[11] Z. Yan, R. Lu, L. Ding, L. Wang, Z. Zhang, Distinct deformation mechanisms of silicate glasses under nanoindentation: the critical role of structure, J. Appl. Phys. 136 (2024) 245101, https://doi.org/10.1063/5.0244335.
[12] H. Liu, B. Deng, S. Sundararaman, Y. Shi, L. Huang, Understanding the response of aluminosilicate and aluminoborate glasses to sharp contact loading using molecular dynamics simulation, J. Appl. Phys. 128 (2020) 035106, https://doi.org/10.1063/5.0013555.
[13] G. Kermouche, E. Barthel, D. Vandembroucq, Ph. Dubujet, Mechanical modelling of indentation-induced densification in amorphous silica, Acta Mater. 56 (2008) 3222–3228, https://doi.org/10.1016/j.actamat.2008.03.010.
[14] T. Rouxel, H. Ji, J.P. Guin, F. Augereau, B. Rufflé, Indentation deformation mechanism in glass: densification versus shear flow, J. Appl. Phys. 107 (2010) 094903, https://doi.org/10.1063/1.3407559.
[15] A. Winterstein-Beckmann, D. Möncke, D. Palles, E.I. Kamitsos, L. Wondraczek, Raman spectroscopic study of structural changes induced by micro-indentation in low alkali borosilicate glasses, J. Non-Cryst. Solids 401 (2014) 110–114, https://doi.org/10.1016/j.jnoncrysol.2013.12.038.
[16] J. Wu, J. Deubener, J.F. Stebbins, L. Grygarova, H. Behrens, L. Wondraczek, Y. Yue, Structural response of a highly viscous aluminoborosilicate melt to isotropic and anisotropic compressions, J. Chem. Phys. 131 (2009) 104504, https://doi.org/10.1063/1.3223282.
[17] S. Bista, J.F. Stebbins, The role of modifier cations in network cation coordination increases with pressure in aluminosilicate glasses and melts from 1 to 3 GPa, Am. Mineral. 102 (2017) 1657–1666, https://doi.org/10.2138/am-2017-6081.
[18] M. Krstulović, A.D. Rosa, N. Biedermann, T. Irifune, M. Wilke, Structural changes in aluminosilicate glasses up to 164 GPa and the role of alkali, alkaline earth cations and alumina in the densification mechanism, Chem. Geol. 560 (2021) 119980, https://doi.org/10.1016/j.chemgeo.2020.119980.
[19] O. Adjaoud, K. Albe, Nanoindentation of nanoglasses tested by molecular dynamics simulations: influence of structural relaxation and chemical segregation on the mechanical response, Front. Mater. 8 (2021), https://doi.org/10.3389/fmats.2021.664220.
[20] L.V.D. Gammond, A. Zeidler, R.E. Youngman, H.E. Fischer, C.L. Bull, P.S. Salmon, Transformations to the aluminum coordination environment and network polymerization in amorphous aluminosilicates under pressure, J. Chem. Phys. 161 (2024) 074503, https://doi.org/10.1063/5.0218574.
[21] Z. Zhang, S. Ispas, W. Kob, Origin of the non-linear elastic behavior of silicate glasses, Acta Mater 231 (2022) 117855, https://doi.org/10.1016/j.actamat.2022.117855.
[22] P.F. Green, D.L. Sidebottom, R.K. Brow, J.J. Hudgens, Mechanical relaxation anomalies in mixed alkali oxides, J. Non-Cryst. Solids 231 (1998) 89–98, https://doi.org/10.1016/S0022-3093(98)00447-5.
[23] J.M. Rimsza, R.E. Jones, Inelastic relaxation processes in amorphous sodium silicates, J. Am. Ceram. Soc. 107 (2024) 1883–1894, https://doi.org/10.1111/jace.19435.

[24] K. Januchta, M. Bauchy, R.E. Youngman, S.J. Rzoska, M. Bockowski, M. M. Smedskjaer, Modifier field strength effects on densification behavior and mechanical properties of alkali aluminoborate glasses, Phys. Rev. Mater. 1 (2017) 063603, https://doi.org/10.1103/PhysRevMaterials.1.063603.

[25] S. Striepe, M.M. Smedskjaer, J. Deubener, U. Bauer, H. Behrens, M. Potuzak, R. E. Youngman, J.C. Mauro, Y. Yue, Elastic and micromechanical properties of isostatically compressed soda–lime–borate glasses, J. Non-Cryst. Solids 364 (2013) 44–52, https://doi.org/10.1016/j.jnoncrysol.2013.01.009.

[26] K.G. Aakermann, K. Januchta, J.A.L. Pedersen, M.N. Svenson, S.J. Rzoska, M. Bockowski, J.C. Mauro, M. Guerette, L. Huang, M.M. Smedskjaer, Indentation deformation mechanism of isostatically compressed mixed alkali aluminosilicate glasses, J. Non-Cryst. Solids 426 (2015) 175–183, https://doi.org/10.1016/j.jnoncrysol.2015.06.028.

[27] M. Guerette, M.R. Ackerson, J. Thomas, F. Yuan, E. Bruce Watson, D. Walker, L. Huang, Structure and properties of silica glass densified in cold compression and hot compression, Sci. Rep. 5 (2015) 15343, https://doi.org/10.1038/srep15343.

[28] L. Ding, R. Lu, L. Wang, Q. Zheng, J.C. Mauro, Z. Zhang, Nanoindentation-induced evolution of atomic-level properties in silicate glass: insights from molecular dynamics simulations, J. Am. Ceram. Soc. 107 (2024) 1448–1458, https://doi.org/10.1111/jace.19230.

[29] A. Păduraru, U.G. Andersen, A. Thyssen, N.P. Bailey, K.W. Jacobsen, J. Schiøtz, Computer simulations of nanoindentation in Mg–Cu and Cu–Zr metallic glasses, Model. Simul. Mater. Sci. Eng. 18 (2010) 055006, https://doi.org/10.1088/0965-0393/18/5/055006.

[30] T. Burgess, M. Ferry, Nanoindentation of metallic glasses, Mater. Today 12 (2009) 24–32, https://doi.org/10.1016/S1369-7021(09)70039-2.

[31] D.A. Kilymis, J.M. Delaye, Nanoindentation of pristine and disordered silica: molecular Dynamics simulations, J. Non-Cryst. Solids 382 (2013) 87–94, https://doi.org/10.1016/j.jnoncrysol.2013.10.013.

[32] O. Adjaoud, K. Albe, Nanoindentation of nanoglasses tested by molecular dynamics simulations: influence of structural relaxation and chemical segregation on the mechanical response, Front. Mater. 8 (2021), https://doi.org/10.3389/fmats.2021.664220.

[33] A. Pedone, G. Malavasi, M.C. Menziani, U. Segre, A.N. Cormack, Molecular dynamics studies of stress-strain behavior of silica glass under a tensile load, Chem. Mater. 20 (2008) 4356–4366, https://doi.org/10.1021/cm800413v.

[34] A. Pedone, Properties calculations of silica-based glasses by atomistic simulations techniques: a review, J. Phys. Chem. C 113 (2009) 20773–20784, https://doi.org/10.1021/jp9071263.

[35] A. Pedone, M.C. Menziani, A.N. Cormack, Dynamics of fracture in silica and soda-silicate glasses: from bulk materials to nanowires, J. Phys. Chem. C 119 (2015) 25499–25507, https://doi.org/10.1021/acs.jpcc.5b08657.

[36] Z. Zhang, S. Ispas, W. Kob, Fracture of silicate glasses: microcavities and correlations between atomic-level properties, Phys. Rev. Mater. 6 (2022) 085601, https://doi.org/10.1103/PhysRevMaterials.6.085601.

[37] Z. Zhang, S. Ispas, W. Kob, Roughness and scaling properties of oxide glass surfaces at the nanoscale, Phys. Rev. Lett. 126 (2021) 066101, https://doi.org/10.1103/PhysRevLett.126.066101.

[38] S. Yuan, C.F. Cheung, A. Shokrani, Z. Zhan, C. Wang, Atomic-level flat polishing of polycrystalline diamond by combining plasma modification and chemical mechanical polishing, CIRP Ann. 74 (2025) 441–445, https://doi.org/10.1016/j.cirp.2025.03.024.

[39] A. Pallini, B. Ziebarth, W. Mannstadt, A. Pedone, Pressure-induced structural variations and mechanical behavior of silicate glasses: role of aluminum and sodium, J. Non-Cryst. Solids 647 (2025) 123267, https://doi.org/10.1016/j.jnoncrysol.2024.123267.

[40] A.P. Thompson, H.M. Aktulga, R. Berger, D.S. Bolintineanu, W.M. Brown, P. S. Crozier, P.J. in 't Veld, A. Kohlmeyer, S.G. Moore, T.D. Nguyen, R. Shan, M. J. Stevens, J. Tranchida, C. Trott, S.J. Plimpton, LAMMPS - a flexible simulation tool for particle-based materials modeling at the atomic, meso, and continuum scales, Comput. Phys. Commun. 271 (2022) 108171, https://doi.org/10.1016/j.cpc.2021.108171.

[41] G.J. Martyna, M.L. Klein, M. Tuckerman, Nosé–Hoover chains: the canonical ensemble via continuous dynamics, J. Chem. Phys. 97 (1992) 2635–2643, https://doi.org/10.1063/1.463940.

[42] M. Bertani, M.C. Menziani, A. Pedone, Improved empirical force field for multicomponent oxide glasses and crystals, Phys. Rev. Mater. 5 (2021) 045602, https://doi.org/10.1103/PhysRevMaterials.5.045602.

[43] A. Pallini, M. Bertani, D. Rustichelli, B. Ziebarth, W. Mannstadt, A. Pedone, Comparison of five empirical potential models for aluminosilicate systems: albite and anorthite as test cases, J. Non-Cryst. Solids 615 (2023) 122426, https://doi.org/10.1016/j.jnoncrysol.2023.122426.

[44] A. Pedone, G. Malavasi, M.C. Menziani, A.N. Cormack, U. Segre, A new self-consistent empirical interatomic potential model for oxides, silicates, and silica-based glasses, J. Phys. Chem. B 110 (2006) 11780–11795, https://doi.org/10.1021/jp0611018.

[45] G. Malavasi, A. Pedone, M.C. Menziani, Study of the structural role of gallium and aluminum in 45S5 bioactive glasses by molecular dynamics simulations, J. Phys. Chem. B 117 (2013) 4142–4150, https://doi.org/10.1021/jp400721g.

[46] G. Ori, M. Montorsi, A. Pedone, C. Siligardi, Insight into the structure of vanadium containing glasses: a molecular dynamics study, J. Non-Cryst. Solids 357 (2011) 2571–2579, https://doi.org/10.1016/j.jnoncrysol.2011.02.002.

[47] A. Pedone, M. Bertani, L. Brugnoli, A. Pallini, Interatomic potentials for oxide glasses: past, present, and future, J. Non-Cryst. Solids X 15 (2022) 100115, https://doi.org/10.1016/j.nocx.2022.100115.

[48] M. Bertani, A. Pallini, M. Cocchi, M.C. Menziani, A. Pedone, A new self-consistent empirical potential model for multicomponent borate and borosilicate glasses, J. Am. Ceram. Soc. 105 (2022) 7254–7271, https://doi.org/10.1111/jace.18681.

[49] A. Pedone, V. Cannillo, M.C. Menziani, Toward the understanding of crystallization, mechanical properties and reactivity of multicomponent bioactive glasses, Acta Mater. 213 (2021) 116977, https://doi.org/10.1016/j.actamat.2021.116977.

[50] Surface roughness measurement: ISO 25178 introduction, Studylib.Net (2021). https://studylib.net/doc/18366442/introduction-to-surface-roughness-measurement-…2 (accessed November 19, 2025).

[51] W.C. Oliver, G.M. Pharr, Measurement of hardness and elastic modulus by instrumented indentation: advances in understanding and refinements to methodology, J. Mater. Res. 19 (2004) 3–20, https://doi.org/10.1557/jmr.2004.19.1.3.

[52] J. Tersoff, Chemical order in amorphous silicon carbide, Phys. Rev. B 49 (1994) 16349–16352, https://doi.org/10.1103/PhysRevB.49.16349.

[53] D.W. Brenner, O.A. Shenderova, J.A. Harrison, S.J. Stuart, B. Ni, S.B. Sinnott, A second-generation reactive empirical bond order (REBO) potential energy expression for hydrocarbons, J. Phys. Condens. Matter 14 (2002) 783, https://doi.org/10.1088/0953-8984/14/4/312.

[54] I.I. Oleinik, D.G. Pettifor, Analytic bond-order potentials beyond Tersoff-Brenner. II. Application to the hydrocarbons, Phys. Rev. B 59 (1999) 8500–8507, https://doi.org/10.1103/PhysRevB.59.8500.

[55] C.J. Fennell, J.D. Gezelter, Is the Ewald summation still necessary? Pairwise alternatives to the accepted standard for long-range electrostatics, J. Chem. Phys. 124 (2006) 234104, https://doi.org/10.1063/1.2206581.

[56] D. Wolf, P. Keblinski, S.R. Phillpot, J. Eggebrecht, Exact method for the simulation of coulombic systems by spherically truncated, pairwise r−1 summation, J. Chem. Phys. 110 (1999) 8254–8282, https://doi.org/10.1063/1.478738.

[57] L. Ding, R. Lu, L. Wang, Q. Zheng, J.C. Mauro, Z. Zhang, Nanoindentation-induced evolution of atomic-level properties in silicate glass: insights from molecular dynamics simulations, J. Am. Ceram. Soc. 107 (2024) 1448–1458, https://doi.org/10.1111/jace.19230.

[58] W.C. Oliver, G.M. Pharr, An improved technique for determining hardness and elastic modulus using load and displacement sensing indentation experiments, J. Mater. Res. 7 (1992) 1564–1583, https://doi.org/10.1557/JMR.1992.1564.

[59] D.A. McKeown, F.L. Galeener, G.E. Brown, Raman studies of Al coordination in silica-rich sodium aluminosilicate glasses and some related minerals, J. Non-Cryst. Solids 68 (1984) 361–378, https://doi.org/10.1016/0022-3093(84)90017-6.

[60] D.A. McKeown, G.A. Waychunas, G.E. Brown, EXAFS study of the coordination environment of aluminum in a series of silica-rich glasses and selected minerals within the Na2O-Al2O3-SiO2 system, J. Non-Cryst. Solids 74 (1985) 349–371, https://doi.org/10.1016/0022-3093(85)90079-1.

[61] Z. Zhang, S. Ispas, W. Kob, The critical role of the interaction potential and simulation protocol for the structural and mechanical properties of sodosilicate glasses, J. Non-Cryst. Solids 532 (2020) 119895, https://doi.org/10.1016/j.jnoncrysol.2020.119895.

[62] N.P. Mellott, S.L. Brantley, J.P. Hamilton, C.G. Pantano, Evaluation of surface preparation methods for glass, Surf. Interface Anal. 31 (2001) 362–368, https://doi.org/10.1002/sia.971.

[63] J. Hopf, E.M. Pierce, Topography and mechanical property mapping of international simple glass surfaces with atomic force microscopy, Procedia Mater. Sci. 7 (2014) 216–222, https://doi.org/10.1016/j.mspro.2014.10.028.

[64] Z. Zhang, S. Ispas, W. Kob, Surface properties of alkali silicate glasses: influence of the modifiers, J. Chem. Phys. 158 (2023) 244504, https://doi.org/10.1063/5.0155497.

[65] T. Rouxel, J. Jang, U. Ramamurty, Indentation of glasses, Prog. Mater. Sci. 121 (2021) 100834, https://doi.org/10.1016/j.pmatsci.2021.100834.

[66] F.J.P. Sousa, M. Dal Bó, P.O. Guglielmi, R. Janssen, D. Hotza, Characterization of Young's modulus and fracture toughness of albite glass by different techniques, Ceram. Int. 40 (2014) 10893–10899, https://doi.org/10.1016/j.ceramint.2014.03.085.

[67] D.R. Tadjiev, R.J. Hand, Surface hydration and nanoindentation of silicate glasses, J. Non-Cryst. Solids 356 (2010) 102–108, https://doi.org/10.1016/j.jnoncrysol.2009.10.005.

[68] D. Vandembroucq, T. Deschamps, C. Coussa, A. Perriot, E. Barthel, B. Champagnon, C. Martinet, Density hardening plasticity and mechanical ageing of silica glass under pressure: a Raman spectroscopic study, J. Phys. Condens. Matter 20 (2008) 485221, https://doi.org/10.1088/0953-8984/20/48/485221.

[69] M.L. Falk, J.S. Langer, Dynamics of viscoplastic deformation in amorphous solids, Phys. Rev. E 57 (1998) 7192–7205, https://doi.org/10.1103/PhysRevE.57.7192.

[70] A.P. Thompson, S.J. Plimpton, W. Mattson, General formulation of pressure and stress tensor for arbitrary many-body interaction potentials under periodic boundary conditions, J. Chem. Phys. 131 (2009) 154107, https://doi.org/10.1063/1.3245303.

[71] M. Wang, B. Wang, T.K. Bechgaard, J.C. Mauro, S.J. Rzoska, M. Bockowski, M. M. Smedskjaer, M. Bauchy, Crucial effect of angular flexibility on the fracture toughness and nano-ductility of aluminosilicate glasses, J. Non-Cryst. Solids 454 (2016) 46–51, https://doi.org/10.1016/j.jnoncrysol.2016.10.020.

[72] K.E. Kelsey, J.F. Stebbins, J.L. Mosenfelder, P.D. Asimow, Simultaneous aluminum, silicon, and sodium coordination changes in 6 GPa sodium aluminosilicate glasses, Am. Mineral. 94 (2009) 1205–1215, https://doi.org/10.2138/am.2009.3177.

[73] Q. Zhao, M. Guerette, G. Scannell, L. Huang, *In-situ* high temperature Raman and Brillouin light scattering studies of sodium silicate glasses, J. Non-Cryst. Solids 358 (2012) 3418–3426, https://doi.org/10.1016/j.jnoncrysol.2012.04.034.